Planck Cold Clumps in the λ Orionis Complex. II. Environmental Effects on Core Formation

Hee-Weon Yi[1], Jeong-Eun Lee[1] [iD], Tie Liu[2,17] [iD], Kee-Tae Kim[2] [iD], Minho Choi[2], David Eden[3], Neal J. Evans II[2,4,5],
James Di Francesco[6,7], Gary Fuller[8] [iD], N. Hirano[9], Mika Juvela[10], Sung-ju Kang[2] [iD], Gwanjeong Kim[2], Patrick M. Koch[9] [iD],
Chang Won Lee[2,11] [iD], Di Li[12,13] [iD], H.-Y. B. Liu[22], Hong-Li Liu[14,15,16], Sheng-Yuan Liu[9], Mark G. Rawlings[17], I. Ristorcelli[18],
Patrico Sanhueza[19] [iD], Archana Soam[2] [iD], Ken'ichi Tatematsu[19] [iD], Mark Thompson[20], L. V. Toth[21,26], Ke Wang[22] [iD],
Glenn J. White[23,24] [iD], Yuefang Wu[25] [iD], and Yao-Lun Yang[4], [iD]
the JCMT Large Program "SCOPE" Collaboration; TRAO Key Science Program "TOP" Collaboration

[1] School of Space Research, Kyung Hee University, 1732, Deogyeong-daero, Giheung-gu, Yongin-si, Gyeonggi-do 17104, Republic of Korea
[2] Korea Astronomy and Space Science Institute 776, Daedeokdae-ro, Yuseong-gu, Daejeon, Republic of Korea
[3] Astrophysics Research Institute, Liverpool John Moores University, IC2, Liverpool Science Park, 146 Brownlow Hill, Liverpool L3 5RF, UK
[4] Department of Astronomy, The University of Texas at Austin, 2515 Speedway, Stop C1400, Austin, TX 78712-1205, USA
[5] Humanitas College, Global Campus, Kyung Hee University, Yongin-shi 17104, Republic of Korea
[6] NRC Herzberg Astronomy and Astrophysics, 5071 West Saanich Road, Victoria, BC V9E 2E7, Canada
[7] Department of Physics and Astronomy, University of Victoria, Victoria, BC V8P 1A1, Canada
[8] UK ALMA Regional Centre Node, Jodrell Bank Centre for Astrophysics, School of Physics and Astronomy, The University of Manchester, Oxford Road,
Manchester M13 9PL, UK
[9] Institute of Astronomy and Astrophysics, Academia Sinica. 11F of Astronomy-Mathematics Building, AS/NTU No.1, Sec. 4, Roosevelt Rd, Taipei 10617, Taiwan,
R.O.C
[10] Department of Physics, P.O.Box 64, FI-00014, University of Helsinki, Finland
[11] University of Science & Technology, 176 Gajeong-dong, Yuseong-gu, Daejeon, Republic of Korea
[12] CAS Key Laboratory of FAST, National Astronomical Observatories, Chinese Academy of Sciences, Beijing, 100012, People's Republic of China
[13] University of Chinese Academy of Sciences, No.19(A) Yuquan Road, Shijingshan District, Beijing 100049, People's Republic of China
[14] Department of Physics, The Chinese University of Hong Kong, Shatin, NT, Hong Kong SAR, People's Republic of China
[15] Departamento de Astronomía, Universidad de Concepción, Av. Esteban Iturra s/n, Distrito Universitario, 160-C, Chile
[16] Chinese Academy of Sciences, South America Center for Astronomy, Camino El Observatorio 1515, Las Condes, Santiago, Chile
[17] East Asian Observatory, 660 N. A'ohoku Place, Hilo, HI 96720, USA
[18] IRAP, CNRS (UMR5277), Université Paul Sabatier, 9 avenue du Colonel Roche, BP 44346, F-31028, Toulouse Cedex 4, France
[19] National Astronomical Observatory of Japan, National Institutes of Natural Sciences, 2-21-1 Osawa, Mitaka, Tokyo 181-8588, Japan
[20] Centre for Astrophysics Research, School of Physics Astronomy & Mathematics, University of Hertfordshire, College Lane, Hatfield, AL10 9AB, UK
[21] Eötvös Loránd University, Department of Astronomy, Pázmány Péter sétány 1/A, H-1117, Budapest, Hungary
[22] European Southern Observatory, Karl-Schwarzschild-Str.2, D-85748 Garching bei München, Germany
[23] Department of Physics and Astronomy, The Open University, Walton Hall, Milton Keynes, MK7 6AA, UK
[24] RAL Space, STFC Rutherford Appleton Laboratory, Chilton, Didcot, Oxfordshire, OX11 0QX, UK
[25] Department of Astronomy, Peking University, 100871, Beijing, People's Republic of China
[26] Konkoly Observatory, Research Centre for Astronomy and Earth Sciences, HAS, Konkoly-Thege M. ut 15-17, 1121 Budapest, Hungary

Abstract

Based on the 850 μm dust continuum data from SCUBA-2 at James Clerk Maxwell Telescope (JCMT), we compare overall properties of Planck Galactic Cold Clumps (PGCCs) in the λ Orionis cloud to those of PGCCs in the Orion A and B clouds. The Orion A and B clouds are well-known active star-forming regions, while the λ Orionis cloud has a different environment as a consequence of the interaction with a prominent OB association and a giant H II region. PGCCs in the λ Orionis cloud have higher dust temperatures ($T_d = 16.13 \pm 0.15$ K) and lower values of dust emissivity spectral index ($\beta = 1.65 \pm 0.02$) than PGCCs in the Orion A ($T_d = 13.79 \pm 0.21$ K, $\beta = 2.07 \pm 0.03$) and Orion B ($T_d = 13.82 \pm 0.19$ K, $\beta = 1.96 \pm 0.02$) clouds. We find 119 substructures within the 40 detected PGCCs and identify them as cores. Out of a total of 119 cores, 15 cores are discovered in the λ Orionis cloud, while 74 and 30 cores are found in the Orion A and B clouds, respectively. The cores in the λ Orionis cloud show much lower mean values of size $R = 0.08$ pc, column density $N(H_2) = (9.5 \pm 1.2) \times 10^{22}$ cm^{-2}, number density $n(H_2) = (2.9 \pm 0.4) \times 10^5$ cm^{-3}, and mass $M_{core} = 1.0 \pm 0.3\,M_\odot$ compared to the cores in the Orion A [$R = 0.11$ pc, $N(H_2) = (2.3 \pm 0.3) \times 10^{23}$ cm^{-2}, $n(H_2) = (3.8 \pm 0.5) \times 10^5$ cm^{-3}, and $M_{core} = 2.4 \pm 0.3\,M_\odot$] and Orion B [$R = 0.16$ pc, $N(H_2) = (3.8 \pm 0.4) \times 10^{23}$ cm^{-2}, $n(H_2) = (15.6 \pm 1.8) \times 10^5$ cm^{-3}, and $M_{core} = 2.7 \pm 0.3\,M_\odot$] clouds. These core properties in the λ Orionis cloud can be attributed to the photodissociation and external heating by the nearby H II region, which may prevent the PGCCs from forming gravitationally bound structures and eventually disperse them. These results support the idea of negative stellar feedback on core formation.

Key words: ISM: clouds – stars: formation – submillimeter: ISM

1. Introduction

Molecular clouds commonly show hierarchical structures, from clumps ($n \sim 10^3$–10^4 cm^{-3}, 0.3–3 pc) down to dense cores ($n \sim 10^4$–10^5 cm^{-3}, 0.03–0.2 pc; Williams et al. 2000; Bergin & Tafalla 2007). Since stars form via the gravitational collapse of the dense cores, it is important to identify the

Table 1
96 PGCCs Observed with SCUBA-2 in the Orion Complex

Cloud	PGCC	R.A.(J2000) (^{h} ^{m} ^{s})	Decl.(J2000) ($^\circ$ $'$ $''$)	Observation	Detection	rms (mJy beam^{-1})
λOrionis	G188.25-12.97	05:17:25.20	+15:04:19.60	SCOPE	No	13.8
	G188.85-13.42	05:17:08.63	+14:19:54.30	SCOPE	No	7.8
	G189.46-10.34	05:29:13.66	+15:29:35.60	SCOPE	No	19.0
	G189.92-14.58	05:15:28.66	+12:49:58.90	SCOPE	No	14.1
	G190.0-13.5A1	05:19:28.09	+13:15:45.30	SCOPE	No	12.0
	G190.12-14.47	05:16:17.78	+12:44:2.60	SCOPE	No	14.7
	G190.15-13.75	05:18:49.36	+13:05:11.80	SCOPE	Yes	8.0
	G190.1-13.7A1	05:18:54.66	+13:02:23.40	SCOPE	No	11.4
	G190.1-14.3A1	05:16:47.16	+12:45:42.50	SCOPE	No	12.8
	G190.36-13.38	05:20:33.62	+13:06:48.90	SCOPE	No	7.8
	G191.03-16.74	05:10:18.90	+10:47:24.00	SCOPE	No	13.1
	G191.04-16.44	05:11:26.74	+10:54:54.60	SCOPE	No	8.5
	G191.18-16.70	05:10:50.72	+10:39:06.80	SCOPE	No	8.5
	G191.69-11.62	05:29:32.36	+12:57:15.40	SCOPE	No	12.9
	G191.90-11.21	05:31:24.92	+12:59:27.00	SCOPE	Yes	12.5
	G192.1-10.9A1	05:32:57.69	+12:57:25.10	SCOPE	Yes	12.3
	G192.12-11.10	05:32:15.03	+12:52:00.20	SCOPE	Yes	13.2
	G192.2-11.3A1	05:31:45.05	+12:34:59.00	SCOPE	No	12.9
	G192.32-11.88	05:29:55.84	+12:17:34.00	SCOPE	Yes	17.0
	G192.36-11.56	05:31:08.65	+12:15:46.20	SCOPE	No	12.8
	G192.45-12.23	05:29:0.18	+12:00:27.60	SCOPE	No	12.2
	G192.5-11.5A1	05:31:30.97	+12:12:12.00	SCOPE	No	13.5
	G192.5-11.5A2	05:31:36.03	+12:18:09.00	SCOPE	No	13.0
	G194.34-16.38	05:18:29.40	+08:15:44.00	SCOPE	No	11.6
	G194.69-16.84	05:17:36.40	+07:44:14.00	SCOPE	No	10.1
	G194.81-15.54	05:22:21.55	+08:19:25.70	SCOPE	No	12, 4
	G194.94-16.74	05:18:26.67	+07:34:12.00	SCOPE	No	11.5
	G194.98-16.96	05:17:47.84	+07:26:22.60	SCOPE	No	8.6
	G195.00-16.95	05:17:47.46	+07:22:08.00	SCOPE	No	9.2
	G195.0-16.4A1	05:20:1.58	+07:39:58.90	SCOPE	No	12.8
	G195.09-16.41	05:20:0.67	+07:39:10.00	SCOPE	No	12.2
	G195.29-15.88	05:22:7.73	+07:44:44.30	SCOPE	No	11.2
	G195.32-16.34	05:20:35.30	+07:28:48.70	SCOPE	No	8.5
	G196.21-15.50	05:25:11.06	+07:10:26.00	SCOPE	No	9.14
	G196.43-16.01	05:23:57.10	+06:43:50.30	SCOPE	No	8.92
	G196.89-16.11	05:24:31.87	+06:18:33.60	SCOPE	No	9.11
	G196.92-10.37	05:44:37.59	+09:10:55.70	SCOPE	Yes	13.8
	G197.12-15.96	05:25:30.06	+06:11:48.90	SCOPE	No	6.72
	G197.13-10.17	05:45:44.66	+09:6:22.70	SCOPE	No	12.4
	G197.18-12.98	05:36:0.38	+07:39:37.70	SCOPE	No	9.28
	G197.46-15.39	05:28:9.30	+06:12:23.20	SCOPE	No	6.71
	G198.03-15.24A	05:29:33.60	+05:52:22.00	SCOPE	No	14.5
	G198.03-15.24B	05:29:49.61	+05:45:50.00	SCOPE	No	11.8
	G198.36-8.88	05:52:41.39	+08:41:16.90	SCOPE	No	12.0
	G198.69-09.12	05:52:29.61	+08:16:45.00	SCOPE	Yes	10.8
	G199.11-10.32	05:49:6.28	+07:20:26.00	SCOPE	No	12.1
	G199.15-10.46	05:48:42.18	+07:14:3.90	SCOPE	No	10.4
	G200.34-10.97	05:49:9.61	+05:55:50.00	SCOPE	Yes	10.9
	G200.47-10.36	05:51:35.27	+06:08:56.70	SCOPE	No	8.4
	G200.48-10.59	05:50:46.63	+06:01:18.20	SCOPE	No	6.6
Orion B	G201.52-11.08	05:51:04.70	+04:53:23.10	SCOPE	Yes	9.4
	G201.72-11.22	05:50:56.64	+04:39:32.20	SCOPE	Yes	8.6
	G203.21-11.20	05:53:46.07	+03:23:41.40	Archive	Yes	15.0
	G204.4-11.3A2	05:55:37.50	+02:11:15.30	SCOPE	Yes	13.0
	G204.61-13.58	05:48:01.64	+01:02:31.20	Archive	No	13.8
	G204.65-14.16	05:46:02.38	+00:43:50.80	Archive	No	13.8
	G204.80-14.35	05:45:39.28	+00:30:34.70	Archive	No	13.8
	G204.8-13.8A1	05:47:26.03	+00:42:47.20	SCOPE	No	11.7
	G204.85-14.07	05:46:43.02	+00:36:13.60	Archive	No	13.8
	G204.97-14.23	05:46:24.24	+00:25:27.40	Archive	No	11.7
	G205.46-14.56	05:46:08.42	−00:11:55.42	Archive	Yes	44.5
	G205.88-16.18	05:41:08.70	−01:16:06.70	Archive	No	13.6
	G206.12-15.76	05:42:45.63	−01:16:14.50	Archive	Yes	13.6

Table 1
(Continued)

Cloud	PGCC	R.A.(J2000) (^{h} ^{m} ^{s})	Decl.(J2000) (° ′ ″)	Observation	Detection	rms (mJy beam^{-1})
	G206.21-16.17	05:41:40.64	−01:34:42.97	Archive	Yes	25.3
	G206.69-16.60	05:40:58.88	−02:08:36.30	Archive	Yes	18.7
	G206.93-16.61	05:41:33.44	−02:18:04.30	Archive	Yes	24.7
Orion A	G207.36-19.82	05:30:47.07	−04:09:45.60	SCOPE	Yes	10.2
	G207.3-19.8A2	05:31:04.07	−04:15:48.00	Archive	Yes	9.8
	G208.68-19.20	05:35:21.95	−05:01:59.60	Archive	Yes	64.2
	G208.89-20.04	05:32:36.76	−05:35:01.46	Archive	Yes	34.1
	G209.05-19.73	05:34:06.48	−05:34:30.40	Archive	Yes	34.1
	G209.29-19.65	05:34:55.50	−05:43:17.70	Archive	Yes	31.3
	G209.55-19.68	05:35:08.71	−05:57:19.80	Archive	Yes	27.6
	G209.77-19.40	05:36:29.17	−06:02:24.75	Archive	Yes	13.9
	G209.77-19.61	05:35:45.13	−06:09:48.77	Archive	Yes	13.9
	G209.79-19.80	05:35:14.59	−06:13:54.77	Archive	Yes	13.9
	G209.94-19.52	05:36:20.04	−06:12:34.86	Archive	Yes	13.9
	G210.20-20.05	05:34:55.10	−06:41:06.50	Archive	No	20.0
	G210.37-19.53	05:37:00.20	−06:36:01.22	Archive	Yes	14.9
	G210.49-19.79	05:36:22.02	−06:45:31.22	Archive	Yes	22.0
	G210.78-19.85	05:36:36.57	−07:05:30.20	Archive	No	16.6
	G210.82-19.47	05:38:00.64	−06:57:17.83	Archive	Yes	15.6
	G210.82-19.70	05:37:13.72	−07:03:12.60	Archive	No	15.6
	G210.97-19.33	05:38:45.67	−06:59:56.82	Archive	Yes	14.3
	G211.01-19.54	05:38:03.19	−07:07:51.18	Archive	Yes	14.9
	G211.16-19.33	05:38:58.55	−07:11:23.12	Archive	Yes	10.3
	G211.47-19.27	05:39:56.46	−07:30:24.31	Archive	Yes	26.1
	G211.72-19.25	05:40:17.99	−07:34:23.00	Archive	Yes	11.0
	G212.10-19.15	05:41:21.44	−07:53:54.70	Archive	Yes	16.4
	G212.84-19.45	05:41:29.52	−08:41:28.00	Archive	Yes	20.0
	G212.90-19.64	05:40:54.33	−08:47:18.90	Archive	No	20.0
	G213.09-19.23	05:42:42.66	−08:46:08.60	Archive	No	20.0
	G213.21-18.31	05:46:16.68	−08:28:26.00	SCOPE	No	15.4
	G213.21-19.84	05:40:41.87	−09:08:32.50	Archive	No	21.1
	G215.44-16.38	05:57:02.78	−09:32:32.80	SCOPE	Yes	9.9
	G215.87-17.62	05:53:14.85	−10:26:33.10	SCOPE	Yes	9.0

gravitationally unstable cores to understand the initial conditions of star formation. Nevertheless, the details of the core formation process are still poorly understood because local environmental conditions, such as turbulence, magnetic field, and radiation, can significantly affect the process of core formation. Therefore, in order to understand the formation of cores, which are formed under these diverse environments, we must perform a statistical study in various environments and in various evolutionary stages.

Orion Molecular Cloud Complex is the largest (extend up to 25° or 187 pc) and most massive molecular clouds within 500 pc of the Sun. This region is an important laboratory for investigating core and star formation in a range of environments and hierarchical structures from extended features to isolated objects. There are three clouds from south to north in the Orion complex: the Orion A and B clouds, and the λ Orionis cloud. The λ Orionis cloud, a region known as the "head" of the Orion complex with a distance 380 ± 30 pc, as derived by Hipparcos, (Perryman et al. 1997) and the total molecular mass of $1.4 \times 10^4 M_\odot$ (Lang et al. 2000), has different environments, including local radiation fields and star-forming activity, from the Orion A and B clouds. At the center of the λ Orionis cloud, there is one of the nearest OB associations known as Collinder 69, including at least one O star, λ Ori, with the spectral type of O8 III and an age of about 5.5 Myr (Cunha & Smith 1996; Dolan & Mathieu 2001, 2002).

Stars in this association are unbound due to the rapid removal of molecular gas by a supernova explosion that occurred about 1 Myr ago (Dolan & Mathieu 2001). This might have subsequently led to the formation of the dusty and gaseous ring by making one of the nearest large H II regions. The molecular clumps in the λ Orionis cloud show clear velocity and temperature gradients (Liu et al. 2012, 2016; Goldsmith et al. 2016), hinting at external compression by the H II region. Liu et al. (2016) suggested that star formation in PGCC G192.32-11.88, which is located in the λ Orionis cloud, has been greatly suppressed because of stellar feedback.

The Orion A and B clouds have been extensively studied and are well-known active star-forming regions that contain thousands of young stellar objects (YSOs; Buckle et al. 2012; Megeath et al. 2012; Polychroni et al. 2013) with a distance of ∼ 420 pc (Jeffries 2007; Sandstrom et al. 2007) and a total mass greater than $2 \times 10^5 M_\odot$ (Wilson et al. 2005). Supernova explosions and H II regions are not discovered in these two clouds. Therefore, comparisons of core properties in the Orion molecular cloud complex will provide an important opportunity to study the effect of the strong radiation field on the next generation of star formation.

We have been carrying out a legacy survey of about 1000 Planck Galactic Cold Clumps (PGCCs) in the 850 μm dust continuum, "SCUBA-2 Continuum Observations of Pre-protostellar Evolution" (SCOPE; Liu et al. 2018a; D. Eden et al., in preparation), to

investigate physical conditions of the PGCCs with a high angular resolution of $14\rlap{.}{''}0$; Planck Collaboration et al. 2016. The PGCC catalog lists 13,188 Galactic sources over the whole sky, identified by the *Planck* survey, that have lower temperatures (6–20 K) than their surrounding environments and the interstellar medium, and thus provides a wealth of sources that may be in the early stage of star formation. It was built using the *Planck* data at 353, 545, and 857 GHz, combined with the *Infrared Astronomical Satellite* (*IRAS*) data (Planck Collaboration et al. 2016). Thousands of dense cores within the PGCCs have been identified in the "SCOPE" survey, and most of them are either starless cores or very young protostellar objects (Class 0/I; Liu et al. 2016; Liu et al. 2018b; Kim et al. 2017; Tatematsu et al. 2017; Tang et al. 2018). The submillimeter dust continuum images of PGCCs can provide an opportunity to study the formation and evolution of cores, because the dust continuum is a good tracer of dense and cold regions. Thus, we can explore how dense cores form and how star formation varies as a function of environment.

We present a detailed comparative statistical study of the 850 μm continuum data of 96 PGCCs in the three clouds of the Orion complex incorporated with archival data. We compare their overall features using the 850 μm continuum data and physical properties (e.g., dust temperature and dust opacity spectral index) using the PGCC catalog. Also, we investigate physical properties (size, column density, mass, and number density) of newly identified cores within detected clumps and discuss the differences among three clouds. In Section 2, observations and data are described. In Section 3, we present the results of our analyses. We discuss the environmental effect of the λ Orionis cloud and the overall properties of cores in the Orion complex in Section 4. The summary is presented in Section 5.

2. Data

2.1. James Clerk Maxwell Telescope (JCMT)/SCUBA-2

As part of the legacy survey, SCOPE (proposal code: M16AL003), we observed 58 PGCCs in the "CV Daisy" mapping mode (Bintley et al. 2014), which is suitable for small and compact sources with sizes of less than $3'$ at 450 and 850 μm with the Submillimetre Common-User Bolometer Array 2 (SCUBA-2) at the 15 m JCMT (Holland et al. 2013). The observed PGCCs consist of 50 in the λ Orionis cloud and 8 in the Orion A and B clouds. Our observations were carried out under weather band 3/4, which maintains 225 GHz opacity ranging from 0.12 to 0.2. This weather condition is not sufficient to obtain 450 μm continuum data due to poor atmospheric transmission. The 450 μm continuum emission thus was not detected toward any of the 58 PGCCs. The map size is $\sim 12' \times 12'$ and the beam size of SCUBA-2 is $14\rlap{.}{''}0$ at 850 μm (Holland et al. 2013). The observed continuum data were reduced using an iterative map-making technique, ORAC-DR, in the STARLINK package, developed by the Joint Astronomy Centre. The reduction is tailored to filter out scales larger than $200''$ on a $4''$ pixel size. We also included archival data of 38 PGCCs located in the Orion A and B clouds from the JCMT Science Archive hosted by the Canadian Astronomical Data Centre (CADC). Table 1 lists information about the 96 PGCCs ,including coordinates, notes for detection, and rms noise level of each SCUBA-2 image.

2.2. Auxiliary Infrared Data

We included the data from the *Wide-Field Infrared Survey Explorer* (*WISE*) AllWISE catalog (Wright et al. 2010), which mapped the whole sky in four mid-infrared bands at 3.4, 4.6, 12, and 22 μm to study an association of any infrared (IR) source within each PGCC. From the data, embedded protostars were identified and their evolutionary stages were classified as described in Section 3.3.1.

3. Results

3.1. SCUBA-2 Observational Results: Detection and Morphology

We obtained the 850 μm maps of 96 PGCCs in the Orion molecular cloud complex either by our own observations or from the JCMT archive, CADC. Fifty PGCCs are located in the λ Orionis cloud, 30 in Orion A, and another 16 in Orion B clouds, respectively. To avoid spurious detections, we adopted $3\sigma_{\rm rms}$ as the minimum significance required for detection. The detected and non-detected PGCCs are marked differently in Figures 1 and 2 as red circles and orange triangles, respectively. Figure 1 marks the locations of selected PGCCs with H_2 column densities greater than $5 \times 10^{20}\,{\rm cm}^{-2}$ ($A_V \sim 0.5$) on top of the *Planck* composite image in the λ Orionis cloud. Figure 2 provides PGCCs in the Orion A and B clouds. We cover all 50 PGCCs with column densities greater than $5 \times 10^{20}\,{\rm cm}^{-2}$ in the λ Orionis cloud from the PGCC catalog, while the PGCCs in the Orion A and B clouds are not fully investigated. The 38 out of 46 PGCCs obtained from the archive have column densities greater than $5 \times 10^{20}\,{\rm cm}^{-2}$, but not all PGCCs with column densities greater than $5 \times 10^{20}\,{\rm cm}^{-2}$ were observed with SCUBA-2. The total numbers of PGCCs with the H_2 column densities greater than $5 \times 10^{20}\,{\rm cm}^{-2}$ are 66 and 68 in the Orion A and B clouds, respectively. Therefore, it is not appropriate to compare detection rates of SCUBA-2 in the three clouds. However, the H_2 column densities of PGCCs are much higher in the Orion A and B clouds (see Table 7), which means these regions are much denser than the λ Orionis cloud.

The overall morphology of PGCCs located in the λ Orionis cloud can be characterized as isolated and compact, while most PGCCs in the Orion A and B clouds are extended and have filamentary structures. The 850 μm dust continuum images also reveal hierarchical structures (see Figures 3–5). Most PGCCs fragment into several substructures, except for four PGCCs (G192.12-11.10, G215.44-16.38, G201.52-11.08, and G206.12-15.76). We performed source fitting to identify and classify the substructures of PGCCs, as will be described in the next section.

3.2. Source Fitting

Source fitting was performed using ClumpFind in the STARLINK package. It is an automatic routine for analyzing clumpy structures. The $5\sigma_{\rm rms}$ detection threshold was used to identify substructures in PGCCs and to determine their sizes. This process contours the data array at many different levels from the peak, and then follows down to a specific minimum contour level defined by users (Williams et al. 1994). Any substructure with values above $5\sigma_{\rm rms}$ is passed to the fitting routine and then the set of pixels is identified as a source.
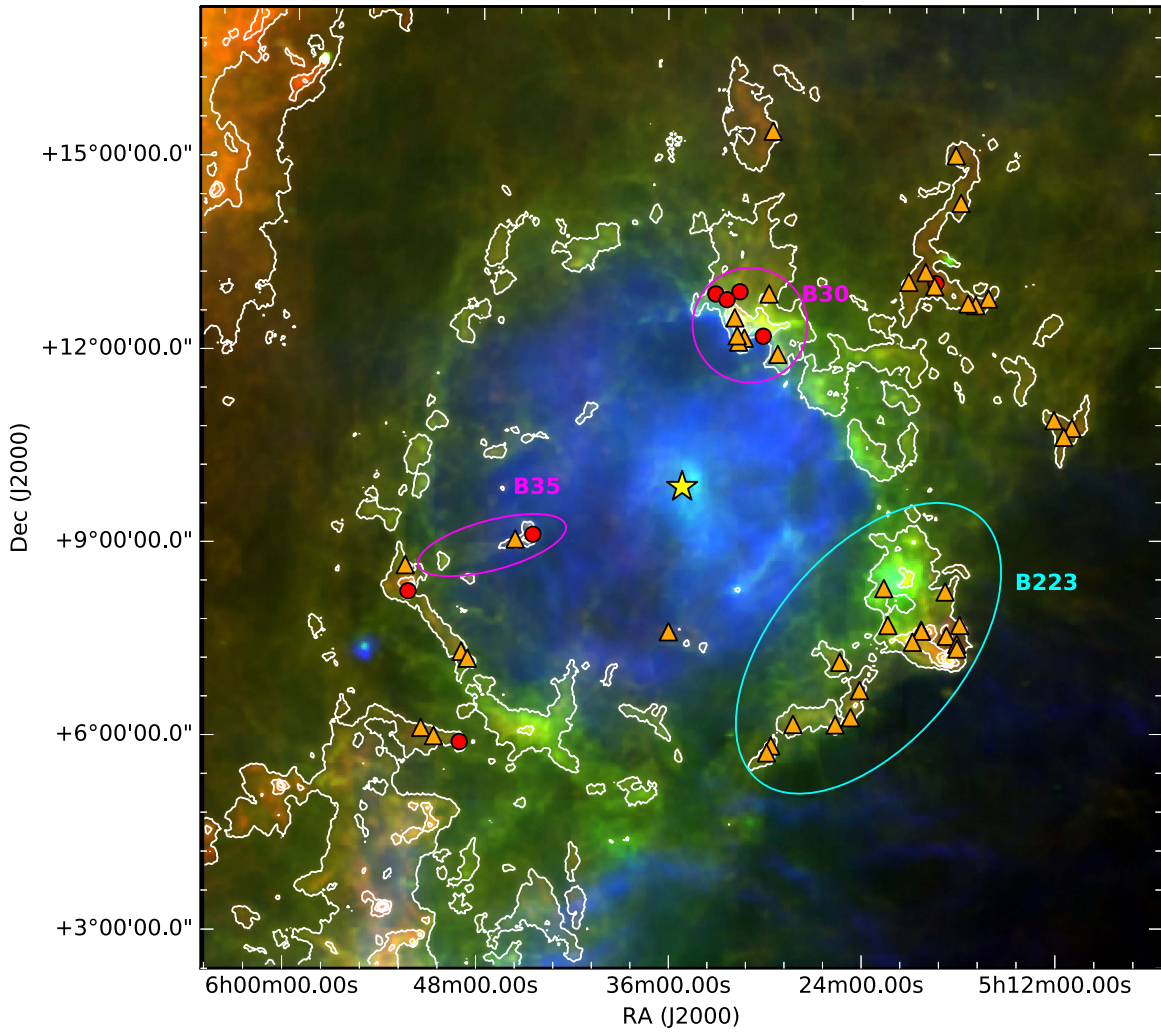
Figure 1. Three-color composite image (red: *Planck* 353 GHz; green: *IRAS* 100 μm; blue: Hα) of the λ Orionis cloud. The white contours show the flux density of *Planck* 857 GHz continuum emission from 20% to 100% in a step of 20% of the peak value 156.4 MJy sr^{-1}. The yellow star indicates the position of the "λ Ori" OB binary. The red circles and orange triangles are all 50 PGCCs with $N(\mathrm{H_2}) > 5 \times 10^{20}$ cm^{-2} in this region. The former are detected at 850 μm, while the latter are not detected. The two types of sub-clouds B30, B35, and B223 are marked with pink ellipses and a cyan ellipse, respectively (see Section 4.2).

Finally, we obtained 119 cores within the 40 detected PGCCs in the Orion complex. In the λ Orionis cloud, there are 8 detected PGCCs, from which 15 cores are identified. The Orion A cloud has 74 cores in 23 PGCCs, and the Orion B cloud has 30 cores in 9 PGCCs. The list of cores in each cloud is found in Tables 2–4.

3.3. Properties of Cores

3.3.1. The H$_2$ Column Density and the Total Mass

For analysis, we assumed that the dust continuum emission is optically thin; thus the continuum emission traces the total mass along the line of sight in the dense parts of PGCCs. The beam-averaged column density is estimated by the equation

$$N(\mathrm{H_2}) = \frac{S'_\nu}{\Omega \mu m_{\mathrm{H}} \kappa_\nu B_\nu(T_{\mathrm{dust}})}, \tag{1}$$

where S'_ν is the beam-averaged flux density per beam, which is integrated over the solid angle defined by $\Omega = (\pi \theta^2_{\mathrm{HPBW}})/(4 \ln 2)$ for a Gaussian aperture, where θ_{HPBW} is the half-power beam width, μ is the mean molecular weight, m_{H} is the mass unit of atomic hydrogen, and $B_\nu(T_{\mathrm{dust}})$ is

the Planck function of dust temperature T_{dust}. We adopted the dust opacity per gram of gas from Beckwith et al. (1990) as $\kappa_\nu = 0.1(\nu/1\,\mathrm{THz})^\beta$ cm^2 g^{-1}, which is appropriate for cores with intermediate and high densities. The T_{dust} and the dust emissivity spectral index β were obtained from the PGCC catalog.

The mean density of the core was calculated using the beam-averaged hydrogen column density

$$n_{\mathrm{H_2}} = \frac{N(\mathrm{H_2})}{R}, \tag{2}$$

where the core diameter R is defined as $R = \sqrt{a \cdot b}$, where again a and b are the major and minor axes (full width at half maximum, FWHM) of the fitting in Section 3.2. The calculated parameters for each source are presented in Tables 2–4.

We estimated the total mass as $M_{\mathrm{total}} = S_\nu D^2/\kappa_\nu B_\nu(T_{\mathrm{dust}})$, where S_ν is the continuum flux density at 850 μm and D is the distance. The median values of column density, number density, mass, and size of cores in each cloud are summarized in Table 5. The median value of column density is the highest in the Orion B cloud (38.4×10^{22} cm^{-2}) and the lowest in the λ Orionis cloud (8.2×10^{22} cm^{-2}). The lowest value is found
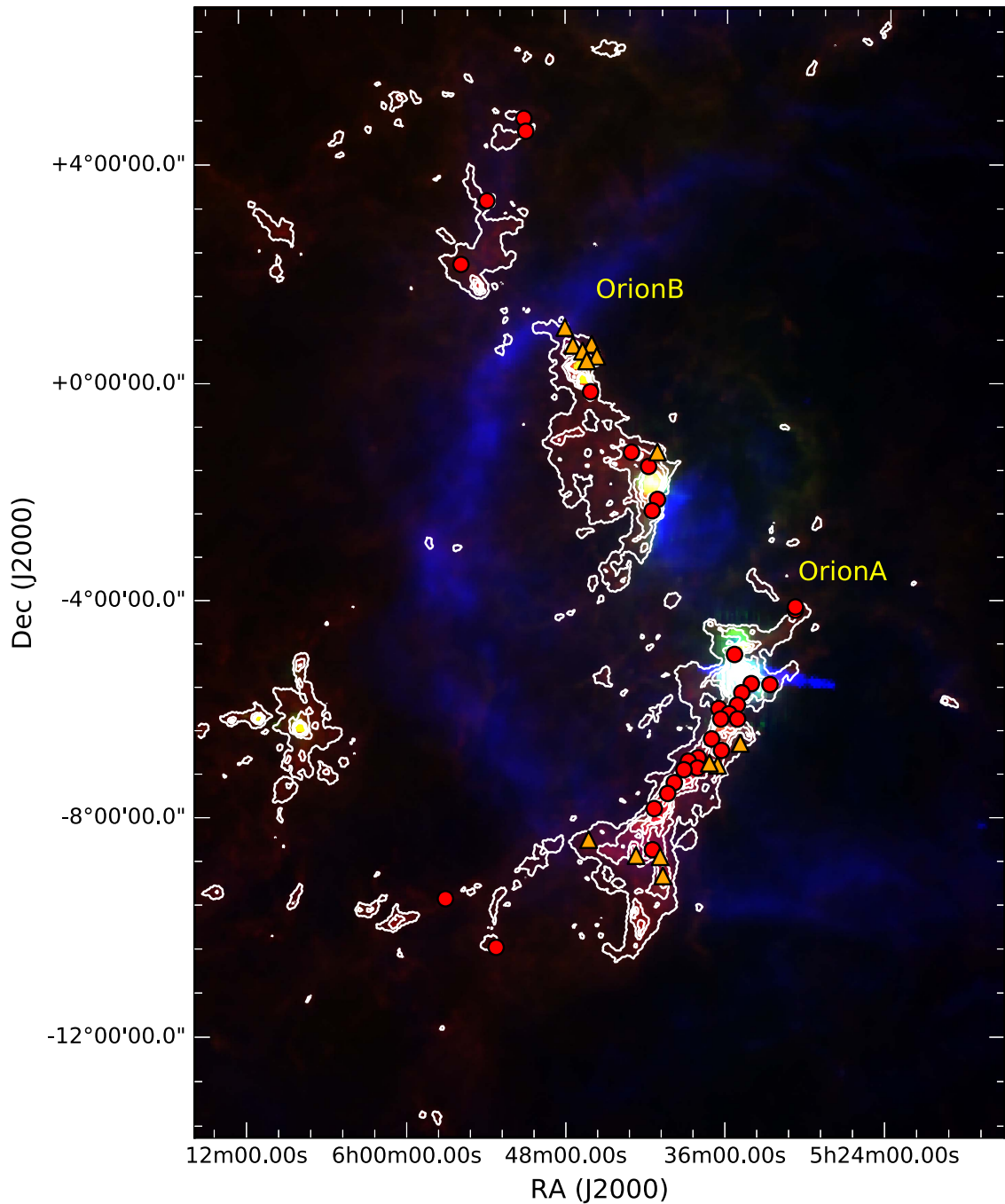
Figure 2. Orion A (lower one) and Orion B (upper one) clouds with 46 PGCCs. The peak intensity is 9122.7 MJy sr^{-1} and the symbols are same as Figure 1.

in the λ Orionis cloud (2.5×10^{22} cm^{-2}), which is about 46.4 times lower than the highest value in the Orion A cloud (116.6×10^{22} cm^{-2}). The derived core masses range from 0.06 to 12.25 $M_{\odot}$. The core with the minimum mass is located in the λ Orionis cloud, while the core with the maximum mass is found in the Orion A cloud. In the median mass, the λ Orionis cloud has the lowest value ($0.77\,M_{\odot}$) and the Orion B cloud has the highest value ($1.81\,M_{\odot}$).

To quantify the differences between cores in the λ Orionis cloud and cores in the Orion A or B clouds, we have calculated the probability of whether these two distributions arise from the same population using the Kolmogorov–Smirnov (K–S) test. The K–S test is a more robust method for measuring the similarity between two distributions than the comparison of the

median and/or mean values. We tested the difference between two distributions under a significance level of 0.05. Two distributions are statistically different when the K–S test gives larger distance values (D_n) than a critical value and smaller p-values than the significance level ($\alpha = 0.05$). Figure 6 shows the results of the K–S test of core masses (upper panels) and column densities (lower panels) of the λ Orionis and Orion A/B clouds in the form of cumulative distribution function. The probability that core masses in the λ Orionis and the Orion A clouds are derived from the same parent population is 0.36%, and only 0.10% for the λ Orionis and Orion B clouds. The probability of the column density distribution of both the Orion A and B clouds originating from the same parent population as the λ Orionis is even lower, at 0.01% (lower panels of
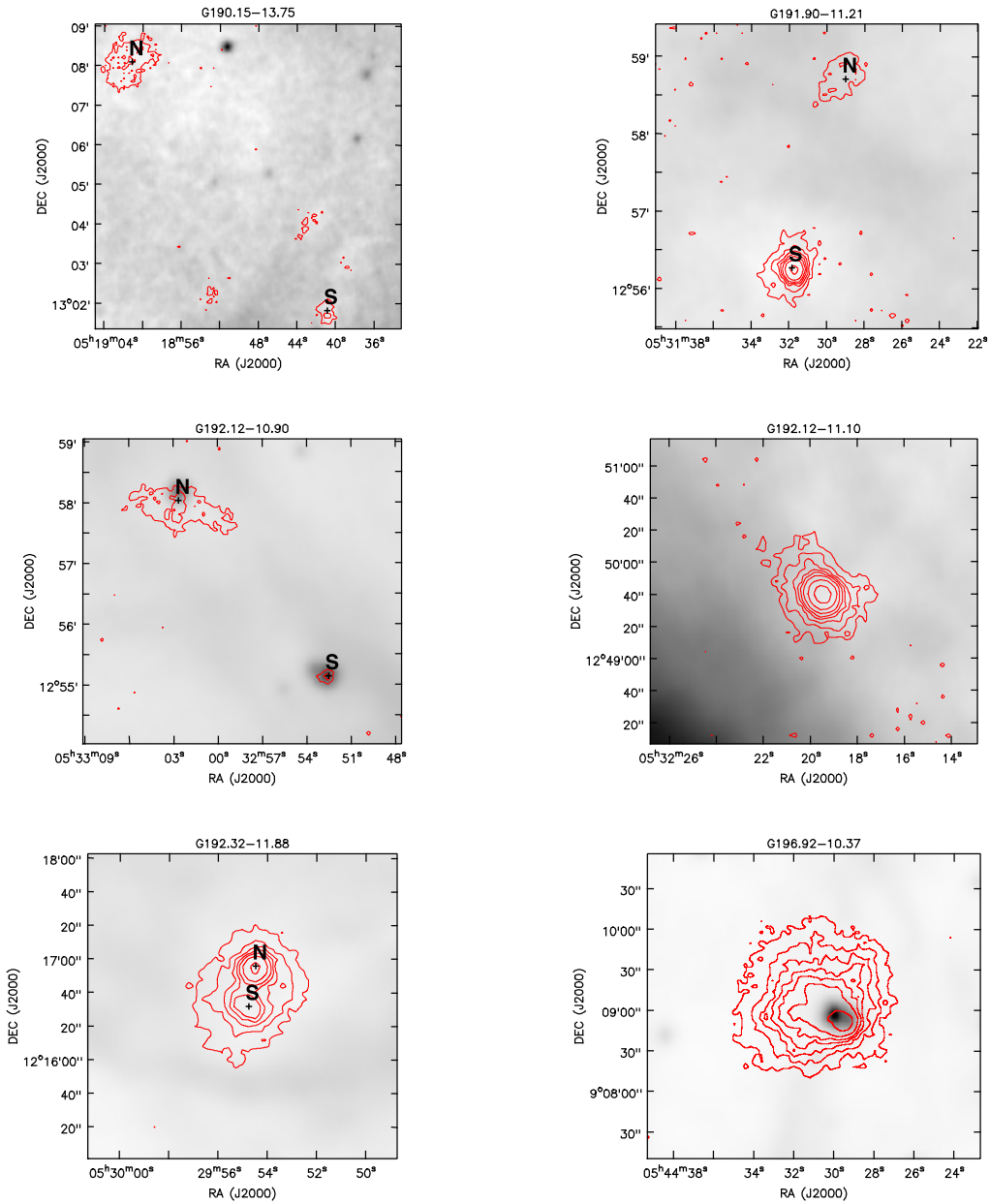
Figure 3. Eight PGCCs detected at 850 μm with SCUBA-2 in the λ Orionis cloud. The 850 μm emission distributions are overlaid on the *WISE* 12 μm images. The red contours represent the 3, 6, 9, 12, 15, 20, and 30$\sigma_{\rm rms}$ levels.

Figure 6). As the *p*-values are lower than the significance level ($\alpha = 0.05$), we can conclude that the distributions of core masses and column densities in the λ Orionis cloud and in the Orion A/B clouds originate from different parent populations.

3.3.2. IR Sources Associated with Cores

Distinguishing protostellar cores from starless cores depends on the detection of embedded infrared sources. Bright emission at 24 μm traces material accreting from the core onto the central protostar; the dust around the protostar can be heated by protostellar luminosity, which mainly arises from accretion shocks (Chambers et al. 2009) . For that reason, if no emission is detected in a core in any of the four *WISE* bands (3.4–22 μm), it is classified as "starless"; otherwise, it is regarded as a candidate for a "protostellar core." However, there are a few difficulties faced when attempting to identify

protostellar cores: deeply embedded sources are too faint to be detected, and many IR sources can be unresolved external galaxies or bright Galactic giant stars, which are positioned by chance along the same line of sight as cores. To avoid these issues, we adopted the "YSO finding scheme" with the *WISE* data by Koenig and Leisawitz (2014); we first excluded extragalactic contaminants such as star-forming galaxies and PAH-feature (polycyclic aromatic hydrocarbons) emissions following their method. As a result, one IR source, which is placed in the inner region of the dashed lines in Figure 7, was removed.

We also attempted to eliminate Active Galactic Nucleus (AGN) contamination using the color–magnitude cut in Koenig and Leisawitz (2014), but found that known YSOs frequently meet this criterion and are hence often misclassified as AGNs. Deeply embedded protostars show faint emission, and they could be removed by the color–magnitude cut. Jørgensen et al.
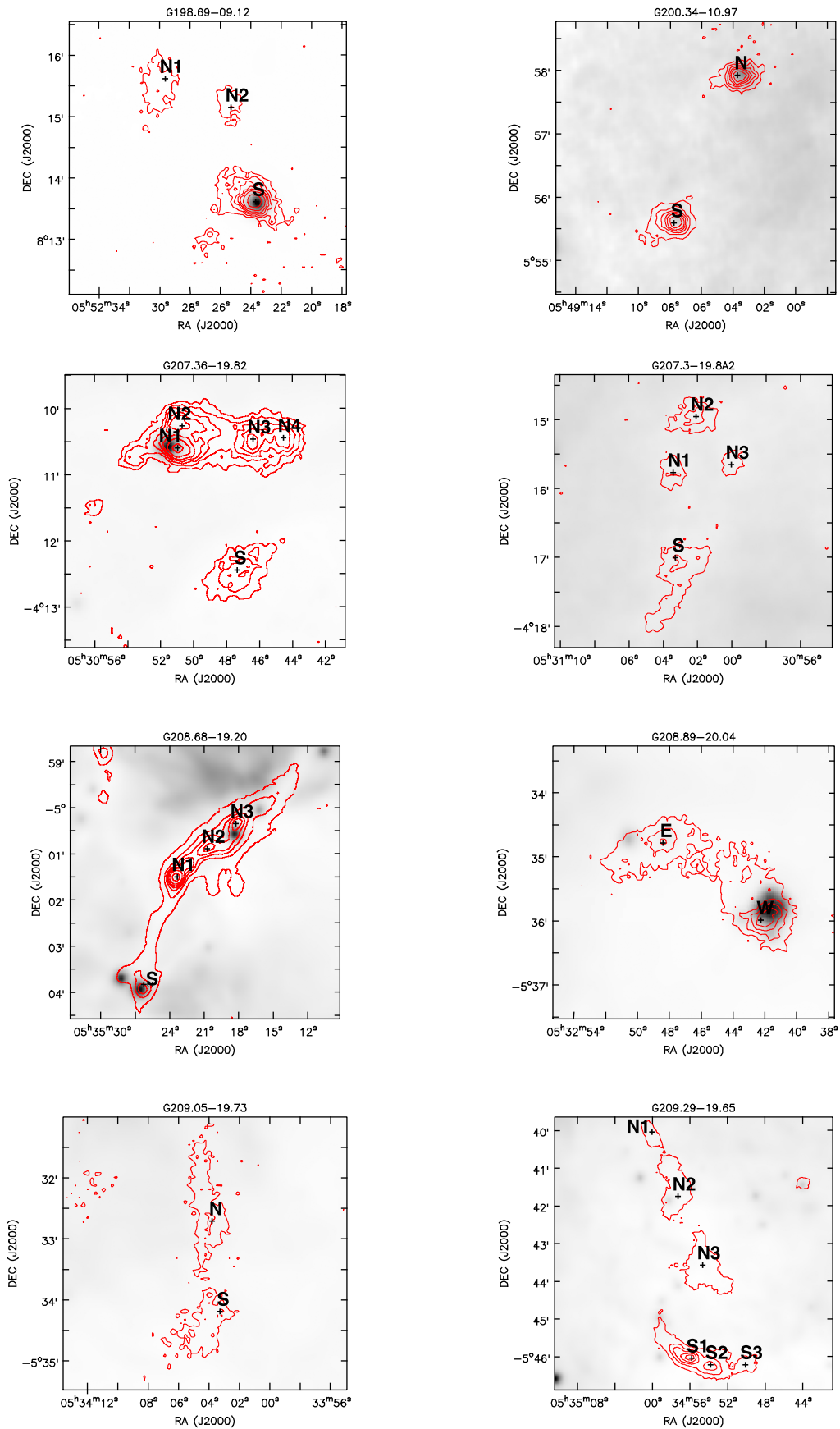
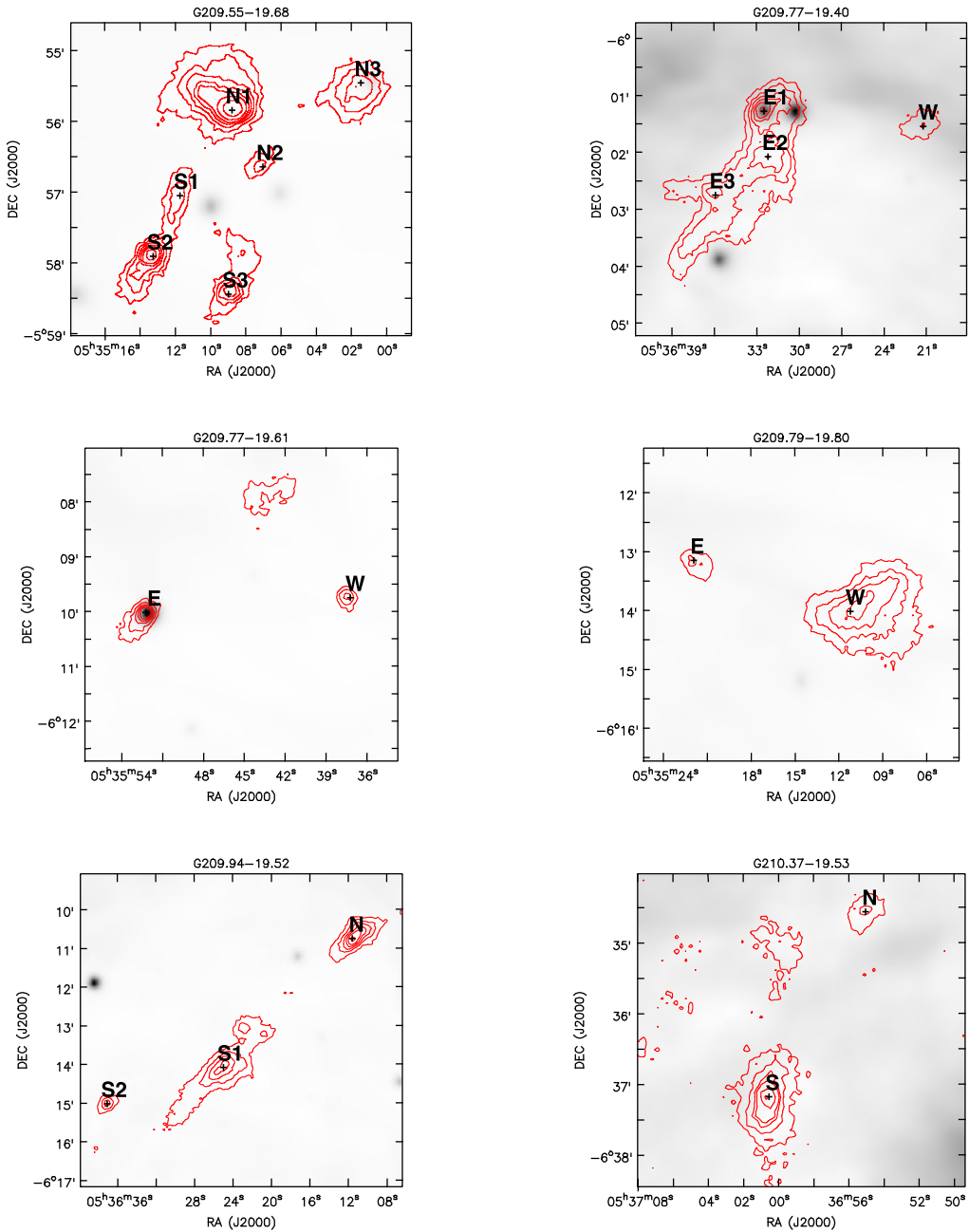**Figure 4.** Same as in Figure 3, except for the 23 PGCCs detected at 850 μm with SCUBA-2 in the Orion A cloud.

Figure 5. Same as in Figure 3, except for the nine PGCCs detected at 850 μm with SCUBA-2 in the Orion B cloud.

(2007) suggested that the possibility of coincidence between an AGN and a core within 15″ is only ∼1% by a random distribution of AGNs.

All IR sources associated with our cores are located within 10″ from the dust continuum peaks. Therefore, we did not apply the AGN cut to identify protostars. Based on this scheme, we identified 5, 22, and 8 YSOs in the λ Orionis, Orion A, and Orion B clouds, respectively. In total, 35 YSOs are associated with PGCCs in the Orion complex.

3.3.3. Classification of YSOs

To study the differences of star formation status among the three clouds, we classified evolutionary stages of the identified 35 YSOs. There are a few physical parameters used in classifying the evolutionary stages of YSOs. First, the most

useful one is the bolometric temperature ($T_{\rm bol}$), which is defined as the temperature of a blackbody with the same flux-weighted mean frequency in the observed SED (Myers & Ladd 1993). It is expected that Class 0 protostar has a $T_{\rm bol} < 70$ K, a Class I protostar has $70\,{\rm K} \leqslant T_{\rm bol} \leqslant 650$ K, and a Class II pre-main-sequence star has $650\,{\rm K} < T_{\rm bol} \leqslant 2800$ K (Chen et al. 1995).

The second one is the near- to mid-infrared spectral index α, which is given as

$$\alpha = \frac{d\,\log(\lambda S(\lambda))}{d\,\log(\lambda)}. \qquad (3)$$

The spectral index calculated in the wavelength range from ∼2 to 20 μm has traditionally been used (Adams et al. 1987; Lada 1987; Andre & Montmerle 1994; Evans et al. 2009; Dunham
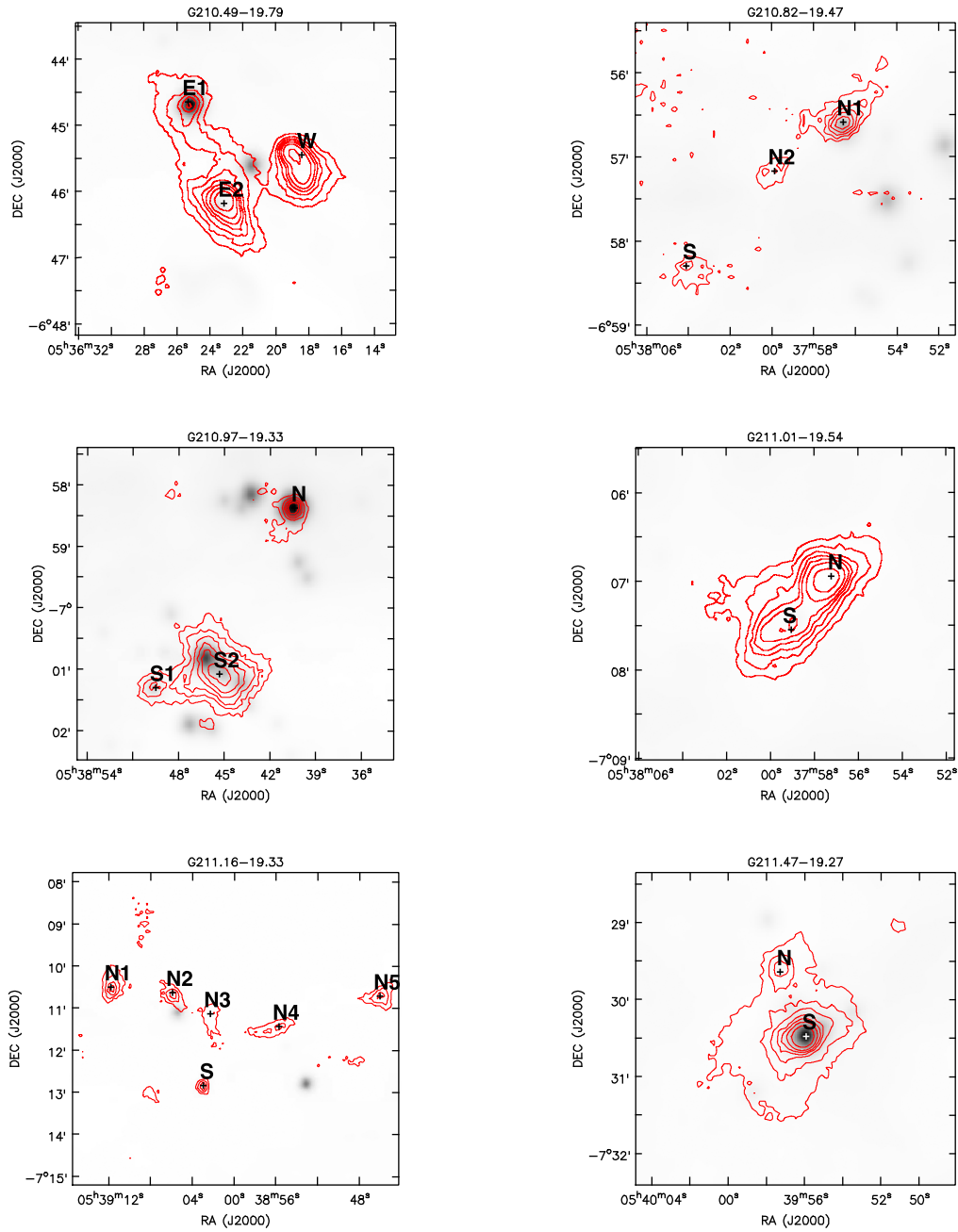
Figure 5. (Continued.)

et al. 2014). The index is $\alpha \geqslant 0.3$ for Class I, $-0.3 < \alpha < 0.3$ for a flat-spectrum source, and $-1.6 < \alpha < -0.3$ for Class II. To classify the evolutionary stages of YSOs, we used the combination of the 4.5–24 μm spectral index ($\alpha_{4.5–24}$) with T_{bol}, as proposed by Furlan et al. (2016): $\alpha_{4.5–24} > 0.3$ and $T_{bol} < 70$ K for Class 0 protostars, $\alpha_{4.5–24} > 0.3$ and 70 K $< T_{bol} < 650$ K for Class I protostars, $-0.3 < \alpha_{4.5–24} < 0.3$ for flat-spectrum sources, and $\alpha_{4.5–24} < -0.3$ and $T_{bol} > 650$ K for Class II pre-main-sequence stars.

We used *WISE* 4.6–22 μm data and SCUBA-2 850 μm peak flux to calculate T_{bol}. In case that a source has a wide range of data including near-infrared data of MIPS of the *Spitzer* and also far-infrared data of *AKARI*, *IRAS*, and *Herschel*, these data points are also included to get more reliable T_{bol} (Adams et al. 1987; Lada 1987; Andre & Montmerle 1994; Evans et al. 2009; Dunham et al. 2014).

Based on this method, five YSOs in the λ Orionis cloud were classified as two Class 0, one Class I, and two flat-spectrum sources. We found six Class 0, eleven Class I, and five flat-spectrum sources in the Orion A cloud, and two Class 0, four Class I, and one flat-spectrum sources in the Orion B cloud (Figure 8). However, because of a lack of far-infrared data for three YSOs in the Orion A cloud, the T_{bol} is probably overestimated, which could result in the misclassification of these sources. The sources that do not have the far-infrared data are marked with asterisks in Figure 8. Table 6 summarizes the numbers of YSOs in each class and the median values of L_{bol}, T_{bol}, and α in each cloud.
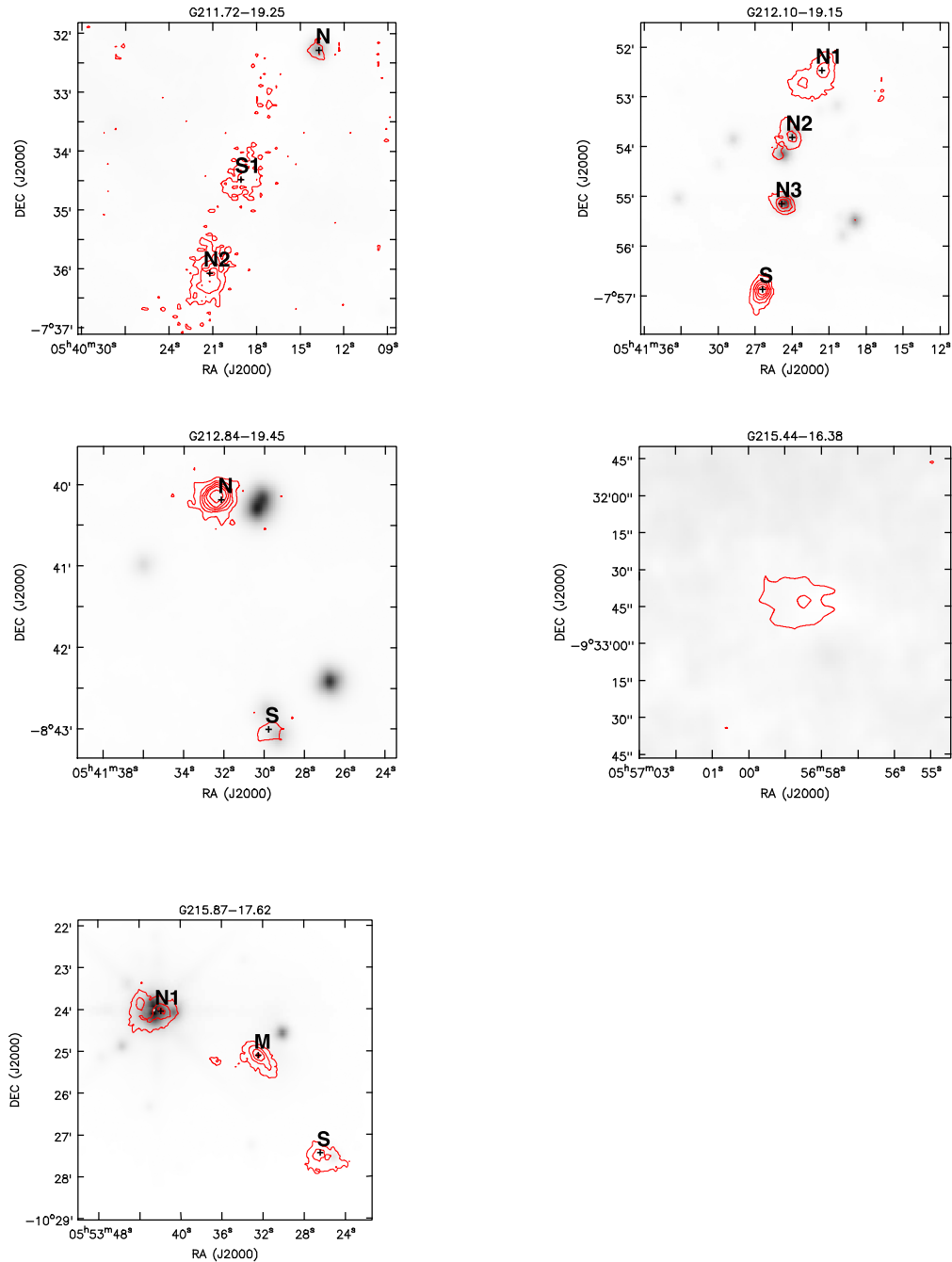
Figure 5. (Continued.)

To confirm whether our classifications of identified YSOs are really reliable, we use the *Spitzer* and *Herschel* protostar catalogs. The *Spitzer Space Telescope* survey identified 3479 YSOs with disks or infalling envelopes in the Orion A and B clouds (Megeath et al. 2012), but did not carry out observations toward the λ Orionis cloud. These YSOs were also observed at 70 and 160 μm, with the Photodetector Array Camera and Spectrometer as part of the Herschel Orion Protostar Survey, and 16 YSOs were newly identified (Stutz et al. 2013; Tobin et al. 2015). We confirmed that all of the 22 YSOs in the Orion A cloud and 7 out of the 8 YSOs in the Orion B cloud identified from the *WISE* data are matched with the YSOs in the *Spitzer* and *Herschel* catalogs within 3″. The one YSO that is not listed in the *Herschel* catalog is thought to be an

Asymptotic Giant Branch (AGB) star or a Classical Be (CBe) star because it was positioned on the boarder of color–magnitude criteria of AGB and CBe stars. AGB stars at great distance are really similar to YSOs, and CBe stars can mimic blue transition disk objects in color–color space (Koenig & Leisawitz 2014). Thus, the YSOs, which reside in a core Middle3 of G205.46-14.56, have a high probability of misclassification, and we do not account this source as a YSO hereafter. This source is marked with a green triangle in Figure 8. Finally, in this study, we identified 5, 22, and 7 YSOs in the λ Orionis, Orion A, and Orion B clouds, respectively, from the *WISE* data. Respectively 10 and 6 YSOs listed in the *Spitzer* and *Herschel* protostar catalogs in the Orion A and B clouds are missed due to lower signal-to-noise ratios and high
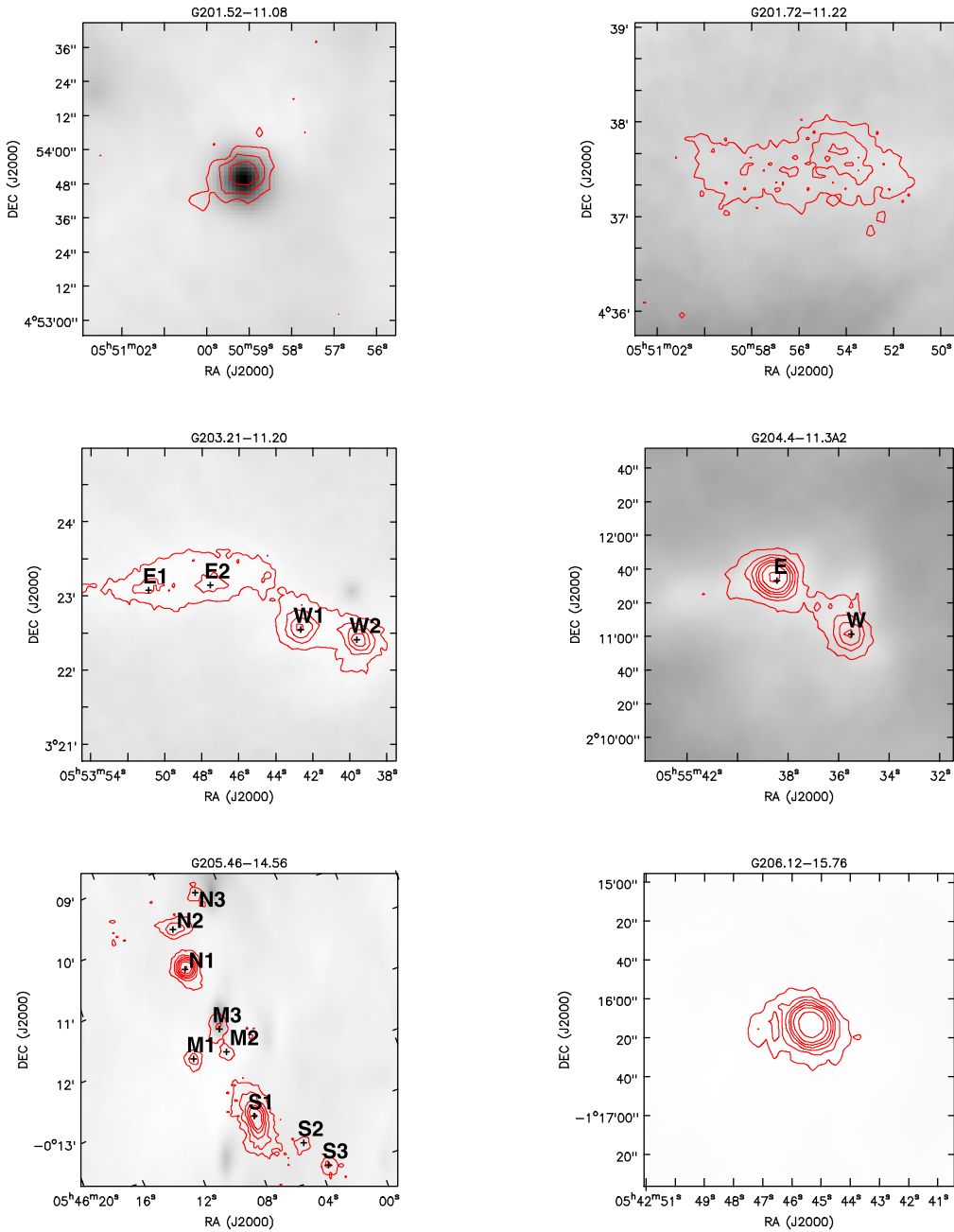
Figure 5. (Continued.)

uncertainties of the Gaussian profile fitting of the *WISE* data. These two parameters given in the AllWISE photometric catalog are important to discriminate between real and fake point sources (Koenig & Leisawitz 2014).

In total, from the *WISE* data, 10 YSOs were identified as Class 0, 16 as Class I, and 8 as flat-spectrum sources. The median $L_{\rm bol}$, $T_{\rm bol}$, and $\alpha_{3.6-22}$ values for the total 34 YSOs are $3.0\,L_\odot$, 150 K, and 1.05, respectively. In the protostellar luminosity study (Kryukova et al. 2012), using the $L_{\rm bol}$ from the c2d survey, the luminosity of YSOs in the Orion A and B clouds peaks near $1\,L_\odot$, while the bolometric luminosity ($L_{\rm bol}$) peaks in this study around $3\,L_\odot$, probably due to the lower sensitivity of *WISE*.

The comparison among three clouds shows that the median $T_{\rm bol}$ of the YSOs in the λ Orionis cloud is 101.7 K, which is lower than that in the Orion A (152.6 K) cloud, and the YSOs in the Orion B cloud have the highest median $T_{\rm bol}$ of 182.8 K (Table 6). This may indicate that the protostars in the λ Orionis cloud are less evolved compared to those in the Orion A and B clouds. $L_{\rm bol}$, $T_{\rm bol}$, $\alpha_{3.6-22}$, and the evolutionary stages of each YSO are listed in the last four columns of Tables 2–4.

3.3.4. Gravitational Instability of Cores

Cores may become gravitationally unstable and subsequently collapse. We investigated whether the starless cores are gravitationally bound and have the ability to form protostars. The Jeans mass is the minimum mass of a spherical portion of a uniform medium that can trigger collapse by its own gravity. The equation of the Jeans mass is adopted from Wang et al.

Table 2
Properties of Cores Detected at 850 μm and Associated YSOs in the λ Orionis Cloud

| PGCC | ID | Classification | R.A.(J2000) (^{h} ^{m} ^{s}) | Decl.(J2000) ($^\circ$ $'$ $''$) | Size (pc) | N_{H_2} (10^{22} cm^{-2}) | n_{H_2} (10^5 cm^{-3}) | M ($M_\odot$) | M_J ($M_\odot$) | Associated YSOs | | | |
										L_{bol} ($L_\odot$)	T_{bol} (K)	$\alpha_{3.6-22}$	Class
G190.15-13.75	North	starless	05:19:01.11	13:08:05.78	0.13	10.6 ± 1.8	3.3 ± 0.6	1.20 ± 0.37	0.19 ± 0.03	⋯	⋯	⋯	⋯
	South	starless	05:18:40.55	13:01:41.64	0.06	10.2 ± 1.3	3.1 ± 0.5	0.25 ± 0.03	0.21 ± 0.05	⋯	⋯	⋯	⋯
G191.90-11.21	North	starless	05:31:28.99	12:58:55.00	0.10	2.5 ± 0.3	0.8 ± 0.2	0.34 ± 0.07	2.66 ± 0.36	⋯	⋯	⋯	⋯
	South	starless	05:31:31.73	12:56:14.99	0.10	7.2 ± 0.5	2.2 ± 0.5	0.89 ± 0.09	0.55 ± 0.14	⋯	⋯	⋯	⋯
G192.12-10.90	North	starless	05:33:02.64	12:57:53.59	0.18	6.1 ± 0.2	1.9 ± 0.3	0.97 ± 0.30	0.59 ± 0.16	⋯	⋯	⋯	⋯
	South	protostellar	05:32:52.52	12:55:08.60	0.04	5.6 ± 0.3	1.7 ± 0.7	0.07 ± 0.01	⋯	2.47 ± 0.17	220.6 ± 7.5	−0.28	flat
G192.12-11.10		starless	05:32:19.54	12:49:40.19	0.12	17.5 ± 1.6	5.4 ± 0.2	2.21 ± 0.33	0.13 ± 0.05	⋯	⋯	⋯	⋯
G192.32-11.88	North	starless	05:29:54.47	12:16:56.00	0.06	11.0 ± 1.9	3.4 ± 0.4	0.49 ± 0.05	0.37 ± 0.09	⋯	⋯	⋯	⋯
	South	starless	05:29:54.74	12:16:32.00	0.05	9.5 ± 1.2	2.9 ± 0.2	0.22 ± 0.02	0.46 ± 0.13	⋯	⋯	⋯	⋯
G196.92-10.37		protostellar	05:44:29.56	09:08:50.20	0.22	18.2 ± 1.3	5.6 ± 0.1	5.41 ± 0.32	⋯	14.87 ± 2.53	67.9 ± 5.0	1.48	0
G198.69-09.12	North1	starless	05:52:29.61	08:15:37.04	0.09	6.4 ± 0.4	2.0 ± 0.4	0.43 ± 0.07	0.46 ± 0.13	⋯	⋯	⋯	⋯
	North2	starless	05:52:25.30	08:15:08.78	0.06	6.7 ± 0.1	2.1 ± 0.4	0.21 ± 0.02	0.43 ± 0.13	⋯	⋯	⋯	⋯
	South	protostellar	05:52:23.66	08:13:37.18	0.12	15.5 ± 1.2	4.8 ± 0.9	1.78 ± 0.25	⋯	18.44 ± 0.39	101.7 ± 2.4	0.82	I
G200.34-10.97	North	protostellar	05:49:03.71	05:57:55.74	0.09	8.2 ± 1.2	2.5 ± 0.6	0.77 ± 0.06	⋯	1.15 ± 0.14	64.8 ± 5.2	1.41	0
	South	protostellar	05:49:07.74	05:55:36.22	0.11	6.9 ± 0.3	2.1 ± 0.5	0.84 ± 0.11	⋯	0.13 ± 0.04	161.3 ± 11.3	0.18	flat

Table 3
Properties of Cores Detected at 850 μm and Associated YSOs in the Orion A Cloud

PGCC	ID	Classification	R.A.(J2000) ($^h\,^m\,^s$)	Decl.(J2000) ($^{\circ}\,'\,''$)	Size (pc)	N_{H2} (10^{22} cm^{-2})	n_{H2} (10^5 cm^{-3})	M ($M_{\odot}$)	M_J ($M_{\odot}$)	Associated YSOs		
										L_{bol} ($L_{\odot}$)	T_{bol} (K)	$\alpha_{3.6-22}$	Class
G207.36-19.82	North1	starless	05:30:50.94	−04:10:35.60	0.06	35.3 ± 3.5	5.7 ± 1.1	1.13 ± 0.46	0.08 ± 0.03	...	...	...	...
	North2	starless	05:30:50.67	−04:10:15.60	0.04	30.0 ± 3.1	4.9 ± 0.9	0.44 ± 0.14	0.11 ± 0.02	...	...	...	...
	North3	starless	05:30:46.40	−04:10:27.60	0.04	25.0 ± 1.8	4.1 ± 0.8	0.47 ± 0.15	0.14 ± 0.08	...	...	...	...
	North4	starless	05:30:44.81	−04:10:27.62	0.03	25.8 ± 1.9	4.2 ± 0.8	0.15 ± 0.05	0.13 ± 0.08	...	...	...	...
	South	starless	05:30:46.81	−04:12:29.39	0.19	6.5 ± 0.4	1.1 ± 0.2	2.01 ± 0.91	1.05 ± 0.13	...	...	...	...
G207.3-19.8A2	North1	starless	05:31:03.40	−04:15:46.00	0.06	7.0 ± 0.5	1.1 ± 0.2	0.16 ± 0.05	0.93 ± 0.40	...	...	...	...
	North2	starless	05:31:02.06	−04:14:57.00	0.08	7.3 ± 0.5	1.2 ± 0.2	0.36 ± 0.18	0.87 ± 0.27	...	...	...	...
	North3	starless	05:30:59.99	−04:15:39.00	0.04	6.4 ± 0.4	1.0 ± 0.2	0.10 ± 0.03	1.07 ± 0.53	...	...	...	...
	South	starless	05:31:03.27	−04:17:00.00	0.16	3.3 ± 0.2	0.5 ± 0.1	0.73 ± 0.08	2.89 ± 1.12	...	...	...	...
G208.68-19.20	North1	starless	05:35:23.37	−05:01:28.70	0.09	108.7 ± 10.8	17.7 ± 3.4	7.60 ± 2.53	0.03 ± 0.02	...	...	...	...
	North2	starless	05:35:20.45	−05:00:52.95	0.05	116.3 ± 19.8	18.9 ± 3.6	2.22 ± 1.15	0.03 ± 0.01	...	...	...	...
	North3	starless	05:35:18.03	−05:00:20.64	0.05	116.6 ± 10.2	18.9 ± 3.7	2.59 ± 1.50	0.03 ± 0.01	...	...	...	...
	South	starless	05:35:26.33	−05:03:56.70	0.09	46.5 ± 4.4	7.6 ± 1.4	3.47 ± 1.03	0.12 ± 0.03	...	...	...	...
G208.89- 20.04	East	protostellar	05:32:48.40	−05:34:47.14	0.13	26.3 ± 2.4	4.3 ± 0.3	3.86 ± 0.29	...	0.60 ± 0.02	308.9 ± 2.6	1.31	I
	West	starless	05:32:42.22	−05:35:58.95	0.18	27.5 ± 2.1	4.5 ± 0.8	8.22 ± 0.15	0.13 ± 0.04	...	...	...	...
G209.05-19.73	North	starless	05:34:03.96	−05:32:42.48	0.23	5.7 ± 0.8	0.9 ± 0.6	2.83 ± 0.15	1.90 ± 1.52	...	...	...	...
	South	starless	05:34:03.12	−05:34:10.98	0.14	9.6 ± 0.9	1.6 ± 0.4	1.65 ± 0.29	0.88 ± 0.07	...	...	...	...
G209.29-19.65	North1	starless	05:35:00.25	−05:40:02.40	0.07	14.7 ± 1.3	2.4 ± 0.8	0.70 ± 0.10	0.54 ± 0.42	...	...	...	...
	North2	starless	05:34:57.30	−05:41:44.40	0.16	12.6 ± 1.5	2.1 ± 0.3	3.05 ± 0.11	0.68 ± 0.23	...	...	...	...
	North3	starless	05:34:54.75	−05:43:34.40	0.19	12.7 ± 1.2	2.1 ± 0.6	4.55 ± 0.57	0.67 ± 0.44	...	...	...	...
	South1	starless	05:34:55.99	−05:46:03.20	0.07	31.3 ± 2.3	5.1 ± 0.4	1.49 ± 0.26	0.17 ± 0.02	...	...	...	...
	South2	starless	05:34:53.81	−05:46:12.80	0.08	38.3 ± 6.3	6.2 ± 0.5	2.31 ± 0.97	0.13 ± 0.06	...	...	...	...
	South3	starless	05:34:49.87	−05:46:11.60	0.06	16.4 ± 2.5	2.7 ± 0.2	0.50 ± 0.05	0.46 ± 0.40	...	...	...	...
G209.55- 19.68	North1	starless	05:35:08.76	−05:55:50.39	0.16	4.1 ± 0.2	0.7 ± 0.1	0.74 ± 0.04	2.67 ± 1.38	...	...	...	...
	North2	starless	05:35:07.01	−05:56:38.39	0.05	19.0 ± 1.2	3.1 ± 0.6	0.28 ± 0.07	0.27 ± 0.07	...	...	...	...
	North3	protostellar	05:35:01.45	−05:55:27.39	0.12	23.3 ± 5.4	3.8 ± 0.5	2.20 ± 0.38	...	0.60 ± 0.01	337.6 ± 3.7	0.42	I
	South1	protostellar	05:35:13.25	−05:57:54.38	0.23	7.6 ± 0.3	1.2 ± 0.2	2.67 ± 0.16	...	1.26 ± 0.06	175.3 ± 6.0	2.67	I
	South2	starless	05:35:11.73	−05:57:02.65	0.12	30.1 ± 13.2	4.9 ± 0.9	1.71 ± 0.16	0.14 ± 0.07	...	...	...	...
	South3	starless	05:35:08.96	−05:58:26.38	0.16	10.0 ± 1.5	1.6 ± 0.5	1.73 ± 0.21	0.70 ± 0.01	...	...	...	...
G209.77-19.40	East1	protostellar	05:36:32.45	−06:01:16.68	0.05	27.8 ± 3.7	4.5 ± 0.6	0.35 ± 0.09	...	0.65 ± 0.02	338.3 ± 4.0	0.56	I
	East2	starless	05:36:32.19	−06:02:04.68	0.07	39.4 ± 4.8	6.4 ± 0.9	1.20 ± 0.56	0.09 ± 0.02	...	...	...	...
	East3	starless	05:36:35.94	−06:02:44.66	0.04	33.3 ± 1.8	5.4 ± 0.7	0.26 ± 0.12	0.11 ± 0.06	...	...	...	...
	West	starless	05:36:21.19	−06:01:32.73	0.09	10.6 ± 2.9	1.7 ± 0.2	0.50 ± 0.07	0.64 ± 0.36	...	...	...	...
G209.77-19.61	East	protostellar	05:35:52.23	−06:10:00.80	0.11	14.8 ± 3.6	2.4 ± 0.2	1.09 ± 0.13	...	17.18 ± 0.26	350.6 ± 8.3	0.22	flat
	West	starless	05:35:37.21	−06:09:44.80	0.06	14.7 ± 1.1	2.4 ± 0.5	0.31 ± 0.17	0.36 ± 0.11	...	...	...	...
G209.79-19.80	East	protostellar	05:35:21.92	−06:13:08.77	0.10	9.8 ± 2.1	1.6 ± 0.2	0.77 ± 0.39	...	0.24 ± 0.05	107.7 ± 9.5	1.01	I
	West	starless	05:35:11.19	−06:14:00.73	0.27	26.9 ± 2.9	4.4 ± 0.4	7.06 ± 2.56	0.15 ± 0.11	...	...	...	...
G209.94-19.52	North	starless	05:36:11.55	−06:10:44.76	0.13	19.1 ± 4.5	3.1 ± 0.5	2.81 ± 0.28	0.33 ± 0.07	...	...	...	...
	South1	starless	05:36:24.96	−06:14:04.71	0.16	15.1 ± 2.9	2.5 ± 0.2	3.52 ± 0.09	0.47 ± 0.08	...	...	...	...
	South2	protostellar	05:36:37.03	−06:15:00.64	0.07	12.0 ± 1.7	1.9 ± 0.8	0.53 ± 0.08	...	0.17 ± 0.02	137.1 ± 16.4	0.05	flat
G210.37-19.53	North	starless	05:36:55.03	−06:34:33.19	0.06	6.7 ± 0.3	1.1 ± 0.2	0.28 ± 0.02	1.26 ± 0.17	...	...	...	...
	South	starless	05:37:00.55	−06:37:10.16	0.15	11.1 ± 0.9	1.8 ± 0.7	2.45 ± 0.23	0.60 ± 0.09	...	...	...	...
G210.49-19.79	East1	protostellar	05:36:25.28	−06:44:42.79	0.10	56.6 ± 10.4	9.2 ± 0.1	2.62 ± 0.13	...	9.35 ± 0.27	699.6 ± 6.8	0.00	flat
	East2	protostellar	05:36:23.13	−06:46:10.79	0.16	83.9 ± 10.1	13.6 ± 0.6	10.36 ± 0.43	...	1.32 ± 0.5	168.1 ± 6.1	1.27	I
	West	protostellar	05:36:18.40	−06:45:26.79	0.11	113.4 ± 13.7	18.4 ± 0.2	7.12 ± 0.25	...	41.62 ± 7.63	51.0 ± 8.8	1.29	0
G210.82-19.47	North1	protostellar	05:37:56.56	−06:56:35.15	0.14	3.8 ± 0.6	0.6 ± 0.6	0.72 ± 0.08	...	1.10 ± 0.06	213.1 ± 8.4	1.22	I
	North2	starless	05:37:59.84	−06:57:09.86	0.06	4.5 ± 0.8	0.7 ± 0.1	0.15 ± 0.05	2.92 ± 0.23	...	...	...	...

Table 3
(Continued)

PGCC	ID	Classification	R.A.(J2000) (h m s)	Decl.(J2000) (° ′ ″)	Size (pc)	$N_{\rm H_2}$ (10^{22} cm^{-2})	$n_{\rm H_2}$ (10^{5} cm^{-3})	M ($M_\odot$)	$M_{\rm J}$ ($M_\odot$)	$L_{\rm bol}$ ($L_\odot$)	$T_{\rm bol}$ (K)	$\alpha_{3.6-22}$	Class
	South	starless	05:38:04.09	−06:58:17.70	0.08	4.1 ± 0.8	0.7 ± 0.8	0.22 ± 0.03	3.29 ± 0.47	⋯	⋯	⋯	⋯
G210.97-19.33	North	protostellar	05:38:40.36	−06:58:21.90	0.12	8.2 ± 0.5	1.3 ± 0.2	0.88 ± 0.22	⋯	22.31 ± 0.32	283.7 ± 6.3	−0.28	flat
	South1	protostellar	05:38:49.46	−07:01:17.90	0.17	21.4 ± 3.4	3.5 ± 0.2	4.63 ± 1.01	⋯	0.73 ± 0.03	208.3 ± 5.5	2.02	I
	South2	starless	05:38:45.30	−07:01:04.41	0.07	12.5 ± 2.8	2.0 ± 0.1	0.40 ± 0.09	0.44 ± 0.07	⋯	⋯	⋯	⋯
G211.01-19.54	North	starless	05:37:57.23	−07:06:56.72	0.10	25.3 ± 1.2	4.1 ± 0.2	2.33 ± 0.36	0.19 ± 0.03	⋯	⋯	⋯	⋯
	South	protostellar	05:37:59.04	−07:07:32.73	0.07	24.5 ± 3.3	4.0 ± 0.1	1.13 ± 0.32	⋯	0.43 ± 0.02	48.3 ± 2.8	1.17	0
G211.16-19.33	North1	protostellar	05:39:11.80	−07:10:29.87	0.11	9.3 ± 0.7	1.5 ± 0.2	0.79 ± 0.05	⋯	0.71 ± 0.05	363.3 ± 21.7	0.54	I
	North2	protostellar	05:39:05.89	−07:10:37.88	0.10	7.5 ± 0.6	1.2 ± 0.2	0.50 ± 0.20	⋯	3.93 ± 0.03	69.9 ± 0.5	2.41	0
	North3	starless	05:39:02.26	−07:11:07.89	0.10	6.2 ± 0.5	1.0 ± 0.1	0.41 ± 0.12	1.20 ± 0.17	⋯	⋯	⋯	⋯
	North4	starless	05:38:55.67	−07:11:25.93	0.13	4.3 ± 0.3	0.7 ± 0.1	0.51 ± 0.04	2.12 ± 0.98	⋯	⋯	⋯	⋯
	North5	starless	05:38:46.00	−07:10:41.90	0.12	7.1 ± 0.5	1.2 ± 0.2	0.64 ± 0.18	0.98 ± 0.16	⋯	⋯	⋯	⋯
	South	protostellar	05:39:02.94	−07:12:49.89	0.06	10.3 ± 1.8	1.7 ± 0.3	0.22 ± 0.10	⋯	4.27 ± 0.14	83.3 ± 2.3	1.14	I
G211.47-19.27	North	starless	05:39:57.27	−07:29:38.28	0.07	40.9 ± 2.6	6.6 ± 0.3	1.66 ± 0.43	0.07 ± 0.01	⋯	⋯	⋯	⋯
	South	starless	05:39:55.92	−07:30:28.28	0.01	71.8 ± 4.7	11.7 ± 0.3	12.25 ± 3.18	0.03 ± 0.01	⋯	⋯	⋯	⋯
G211.72-19.25	North	protostellar	05:40:13.72	−07:32:16.80	0.03	9.1 ± 1.3	1.5 ± 0.5	0.07 ± 0.06	⋯	35.94 ± 0.01	56.4 ± 0.1	0.17	flat
	South1	starless	05:40:19.04	−07:34:28.79	0.12	8.3 ± 1.5	1.3 ± 0.5	1.15 ± 0.82	0.79 ± 0.09	⋯	⋯	⋯	⋯
	South2	starless	05:40:21.18	−07:34:04.00	0.10	6.8 ± 0.5	1.1 ± 0.4	0.62 ± 0.21	1.07 ± 0.11	⋯	⋯	⋯	⋯
G212.10-19.15	North1	starless	05:41:21.56	−07:52:27.66	0.18	19.0 ± 1.4	3.1 ± 0.4	3.52 ± 1.68	0.18 ± 0.03	⋯	⋯	⋯	⋯
	North2	starless	05:41:23.98	−07:53:48.49	0.12	18.1 ± 1.4	2.9 ± 0.4	1.65 ± 0.72	0.19 ± 0.04	⋯	⋯	⋯	⋯
	North3	protostellar	05:41:24.82	−07:55:08.48	0.11	20.2 ± 1.5	3.3 ± 0.4	1.36 ± 0.78	⋯	9.06 ± 0. 05	85.7 ± 0.9	1.87	I
	South	protostellar	05:41:26.39	−07:56:51.81	0.15	18.6 ± 1.3	3.0 ± 0.4	2.41 ± 1.00	⋯	1.66 ± 0.16	50.6 ± 1.3	0.87	0
G212.84-19.45	North	protostellar	05:41:32.14	−08:40:10.94	0.10	19.7 ± 1.4	3.2 ± 0.5	1.36 ± 0.50	⋯	3.63 ± 0.02	48.2 ± 0.3	0.64	0
	South	protostellar	05:41:29.70	−08:43:00.22	0.09	6.8 ± 0.4	1.1 ± 0.2	0.32 ± 0.11	⋯	7.09 ± 1.30	56.9 ± 4.1	1.60	0
G215.44-16.38		starless	05:56:58.45	−09:32:42.30	0.06	6.0 ± 0.4	1.0 ± 0.2	0.19 ± 0.04	1.21 ± 0.16	⋯	⋯	⋯	⋯
G215.87-17.62	North	starless	05:53:41.91	−10:24:02.00	0.26	6.1 ± 0.4	1.0 ± 0.2	4.05 ± 0.84	1.18 ± 0.16	⋯	⋯	⋯	⋯
	Middle	starless	05:53:32.41	−10:25:06.07	0.24	4.9 ± 0.3	0.8 ± 0.1	2.69 ± 0.64	1.68 ± 0.18	⋯	⋯	⋯	⋯
	South	starless	05:53:26.43	−10:27:26.02	0.20	5.8 ± 0.4	0.9 ± 0.1	2.23 ± 0.69	1.28 ± 0.16	⋯	⋯	⋯	⋯

Table 4
Properties of Cores Detected at 850 μm and Associated YSOs in the Orion B Cloud

| PGCC	ID	Classification	R.A.(J2000) (^{h} ^{m} ^{s})	Decl.(J2000) ($^\circ$ $'$ $''$)	Size (pc)	N_{H_2} (10^{22} cm^{-2})	n_{H_2} (10^5 cm^{-3})	M ($M_\odot$)	M_J ($M_\odot$)	Associated YSOs L_{bol} ($L_\odot$)	T_{bol} (K)	$\alpha_{3.6-22}$	Class
G201.52-11.08		protostellar	05:50:59.01	04:53:53.10	0.05	7.9 ± 0.5	3.3 ± 0.8	0.14 ± 0.04	⋯	3.03 ± 0.37	66.4 ± 3.9	1.00	0
G201.72-11.22		starless	05:50:54.53	04:37:42.60	2.25	3.2 ± 0.2	1.3 ± 0.4	1.83 ± 0.21	0.87 ± 0.37	⋯	⋯	⋯	⋯
G203.21-11.20	East1	starless	05:53:51.11	03:23:04.90	0.12	23.9 ± 3.5	9.8 ± 0.6	2.50 ± 0.43	0.03 ± 0.01	⋯	⋯	⋯	⋯
	East2	starless	05:53:47.90	03:23:08.90	0.12	25.0 ± 3.7	10.3 ± 0.7	2.65 ± 1.73	0.03 ± 0.01	⋯	⋯	⋯	⋯
	West1	starless	05:53:42.83	03:22:32.90	0.12	26.8 ± 2.7	11.1 ± 1.9	2.81 ± 0.13	0.03 ± 0.01	⋯	⋯	⋯	⋯
	West2	starless	05:53:39.62	03:22:24.90	0.10	32.5 ± 2.8	13.4 ± 1.5	2.51 ± 0.19	0.02 ± 0.01	⋯	⋯	⋯	⋯
G204.4-11.3A2	East	starless	05:55:38.43	02:11:33.30	0.08	47.4 ± 3.4	19.6 ± 1.6	2.97 ± 0.23	0.01 ± 0.01	⋯	⋯	⋯	⋯
	West	starless	05:55:35.49	02:11:01.30	0.05	35.5 ± 1.5	14.7 ± 1.5	0.99 ± 0.24	0.02 ± 0.01	⋯	⋯	⋯	⋯
G205.46-14.56	North1	starless	05:46:05.49	−00:09:32.35	0.03	41.4 ± 2.8	17.0 ± 1.9	0.39 ± 0.06	0.02 ± 0.01	⋯	⋯	⋯	⋯
	North2	protostellar	05:46:07.89	−00:10:01.97	0.06	54.9 ± 3.3	22.6 ± 1.5	1.79 ± 0.38	⋯	15.74 ± 0.13	117.4 ± 1.6	1.08	I
	North3	protostellar	05:46:08.06	−00:10:43.57	0.09	87.0 ± 5.5	35.9 ± 1.7	6.21 ± 1.33	⋯	0.50 ± 0.04	182.8 ± 16.6	1.39	I
	Middle1	starless	05:46:09.65	−00:12:12.92	0.05	54.5 ± 3.3	22.5 ± 1.1	1.04 ± 0.16	0.01 ± 0.01	⋯	⋯	⋯	⋯
	Middle2	starless	05:46:07.49	−00:12:22.42	0.03	46.6 ± 2.9	19.2 ± 1.9	0.48 ± 0.09	0.01 ± 0.01	⋯	⋯	⋯	⋯
	Middle3	starless	05:46:07.37	−00:11:53.35	0.06	47.6 ± 3.1	19.6 ± 1.9	1.36 ± 0.25	0.01 ± 0.01	⋯	⋯	⋯	⋯
	South1	protostellar	05:46:07.11	−00:13:34.57	0.13	66.5 ± 4.3	27.4 ± 1.7	11.35 ± 2.18	⋯	9.66 ± 0.36	19.7 ± 0.7	1.18	0
	South2	protostellar	05:46:04.49	−00:14:18.87	0.03	48.0 ± 3.0	19.8 ± 2.9	0.46 ± 0.10	⋯	23.31 ± 4.19	273.2 ± 5.2	−0.11	flat
	South3	protostellar	05:46:03.54	−00:14:49.34	0.04	49.5 ± 3.1	20.4 ± 1.9	0.86 ± 0.16	⋯	2.95 ± 0.05	346.6 ± 3.1	0.85	I
G206.12-15.76		starless	05:42:45.27	−01:16:11.37	0.14	26.3 ± 2.1	10.8 ± 1.3	3.86 ± 1.73	0.03 ± 0.01	⋯	⋯	⋯	⋯
G206.21-16.17	North	starless	05:41:39.28	−01:35:52.86	0.21	11.5 ± 2.8	4.7 ± 0.8	4.97 ± 0.05	0.17 ± 0.09	⋯	⋯	⋯	⋯
	South	starless	05:41:34.23	−01:37:28.76	0.11	8.7 ± 0.2	3.6 ± 0.8	1.05 ± 0.46	0.25 ± 0.09	⋯	⋯	⋯	⋯
G206.69-16.60	North	starless	05:40:58.08	−02:07:28.29	0.10	8.0 ± 0.6	3.3 ± 0.8	0.75 ± 0.03	0.32 ± 0.08	⋯	⋯	⋯	⋯
	South	starless	05:40:58.62	−02:08:40.72	0.17	12.4 ± 1.5	5.1 ± 0.5	3.48 ± 0.11	0.17 ± 0.10	⋯	⋯	⋯	⋯
G206.93-16.61	East1	starless	05:41:40.54	−02:17:04.29	0.12	41.3 ± 6.6	17.1 ± 2.9	5.37 ± 0.54	0.03 ± 0.01	⋯	⋯	⋯	⋯
	East2	protostellar	05:41:37.32	−02:17:16.29	0.10	45.5 ± 3.4	18.8 ± 2.4	4.29 ± 0.16	⋯	38.23 ± 3.79	250.9 ± 3.9	1.48	I
	West1	starless	05:41:25.57	−02:16:04.30	0.08	24.4 ± 3.8	10.1 ± 2.3	1.55 ± 0.23	0.06 ± 0.02	⋯	⋯	⋯	⋯
	West2	starless	05:41:26.39	−02:18:16.40	0.04	64.2 ± 9.3	26.5 ± 2.3	1.37 ± 0.23	0.01 ± 0.01	⋯	⋯	⋯	⋯
	West3	starless	05:41:25.04	−02:18:08.11	0.06	99.1 ± 1.9	40.8 ± 4.7	3.38 ± 0.15	0.01 ± 0.01	⋯	⋯	⋯	⋯
	West4	starless	05:41:25.84	−02:19:28.42	0.08	21.9 ± 1.5	9.0 ± 0.2	1.25 ± 0.67	0.07 ± 0.02	⋯	⋯	⋯	⋯
	West5	starless	05:41:28.77	−02:20:04.30	0.11	57.0 ± 3.6	23.5 ± 1.6	7.10 ± 0.72	0.02 ± 0.01	⋯	⋯	⋯	⋯
	West6	starless	05:41:29.57	−02:21:16.06	0.08	20.1 ± 1.5	8.3 ± 0.9	1.15 ± 0.15	0.08 ± 0.02	⋯	⋯	⋯	⋯
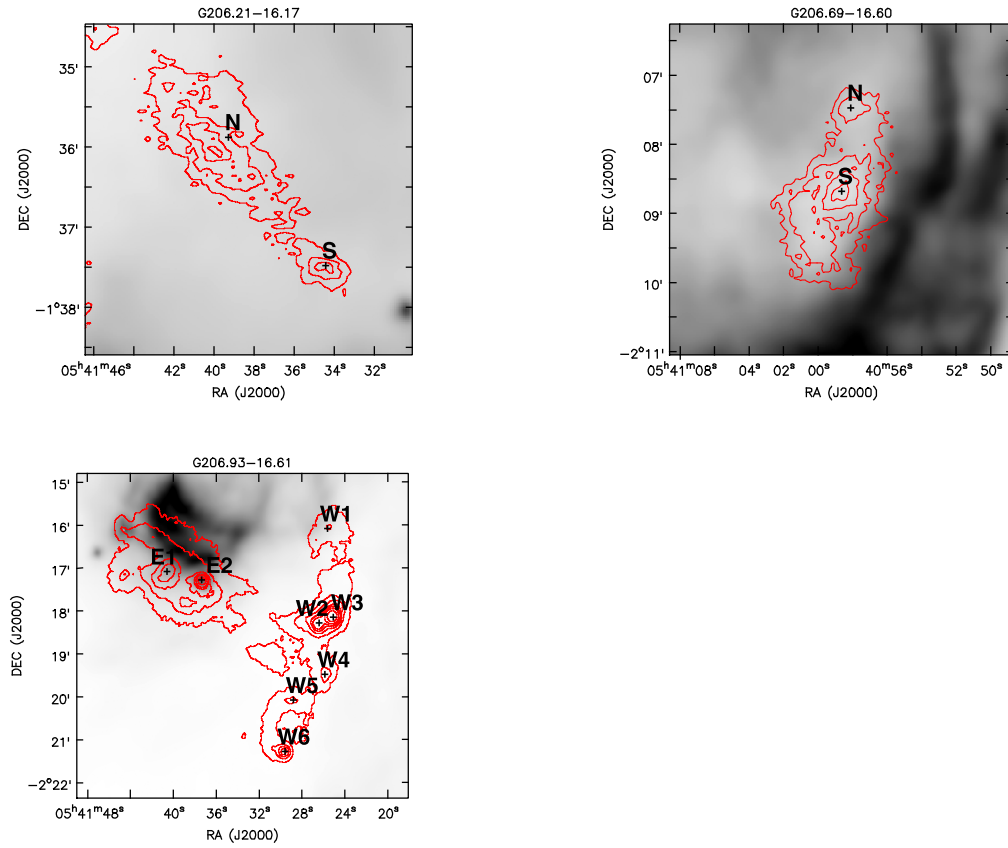
Figure 6. K–S test of core masses and column densities. The upper two panels show cumulative distribution functions (CDF) of core masses. The blue solid lines show the CDF of the λ Orionis cores, and the magenta and green solid lines show the CDF of the Orion A (left) and Orion B (right) cores, respectively. The lower two panels show the CDF of column densities comparing λ Orionis cores to those of Orion A (left) and Orion B (right).

Table 5
Statistics of Core Properties

Cloud	N_{H_2} (10^{22} cm^{-2})				n_{H_2} (10^5 cm^{-3})				Core mass ($M_\odot$)				Core size (pc)			
	Min	Max	Mean	Median	Min	Max	Mean	Median	Min	Max	Mean	Median	Min	Max	Mean	Median
λ Orionis	2.5	18.2	9.5	8.2	0.7	5.6	2.9	2.5	0.06	5.41	1.07	0.77	0.03	0.19	0.08	0.09
Orion A	3.3	116.6	23.4	14.7	0.5	18.9	3.8	3.4	0.07	12.25	2.39	1.18	0.02	0.26	0.11	0.11
Orion B	3.2	99.1	38.4	38.4	1.3	40.8	15.6	15.8	0.14	11.36	2.66	1.81	0.03	2.25	0.16	0.10

(2014):

$$M_J = \frac{\pi^{5/2} c_s^3}{6\sqrt{G^3 \rho}} = 0.877 \left(\frac{T}{10\,\text{K}}\right)^{3/2} \left(\frac{n}{10^5\,\text{cm}^{-3}}\right)^{-1/2} M_\odot, \quad (4)$$

where T is the temperature and n is the H$_2$ volume density, respectively. We assumed that the gas and dust are well coupled in cores with high densities ($n \geqslant 10^5$ cm^{-3}) via collisions (Goldreich & Kwan 1974), and thus their temperatures are the same (Galli et al. 2002). The core mass and its Jeans mass, M and M_J, are listed in Tables 2–4.

Cores with masses greater than their Jeans masses will collapse when we do not consider the effect by the magnetic field or turbulence. Cores with masses less than their Jeans masses are not gravitationally bound and will be dispersed by their own internal motion. In the λ Orionis cloud, there are four starless cores whose Jeans masses are significantly larger than their core masses, suggesting that these starless cores may disperse in the future. The other six starless cores have larger

Table 6
Statistics of YSOs

Cloud	Number of YSOs				L_{bol}[a]	T_{bol}[a]	α[a]
	Total	Class 0	Class I	Flat	($L_\odot$)	(K)	
λ Orionis	5	2	1	2	2.47	101.7	0.82
Orion A	22	6	11	5	1.49	152.6	1.14
Orion B	7	2	4	1	9.66	182.8	1.08

Note.
[a] The median value of all YSOs in a given cloud.

core masses than their Jeans masses. In the Orion A cloud, 37 out of 52 starless cores have masses larger than their Jeans masses, and they may collapse to form protostars. In the case of the Orion B cloud, all the 23 starless cores have masses larger than their Jeans masses. These results are presented in Figure 9. In total, 65 out of 85 starless cores may collapse, while 20 cores remain as starless. The highest and lowest fractions of
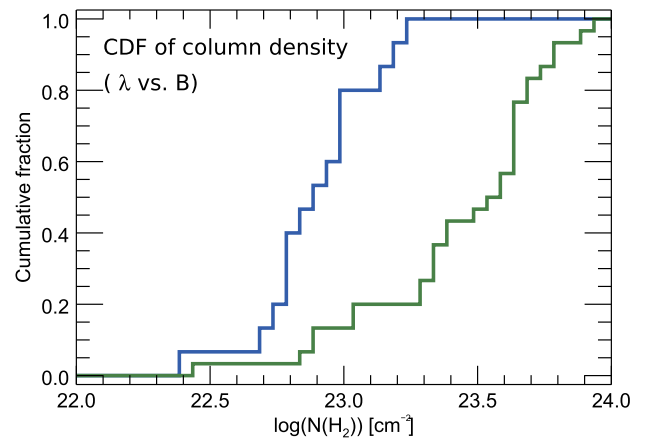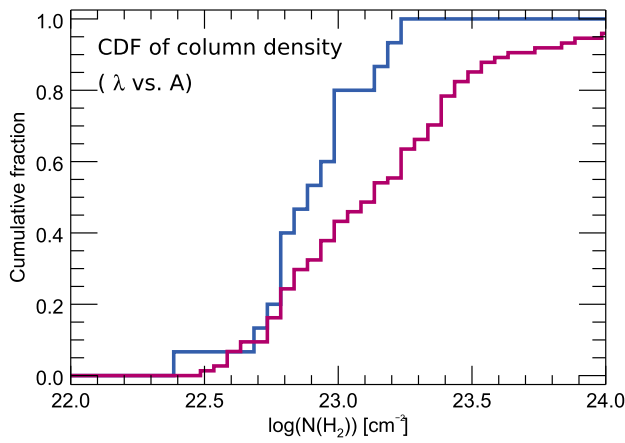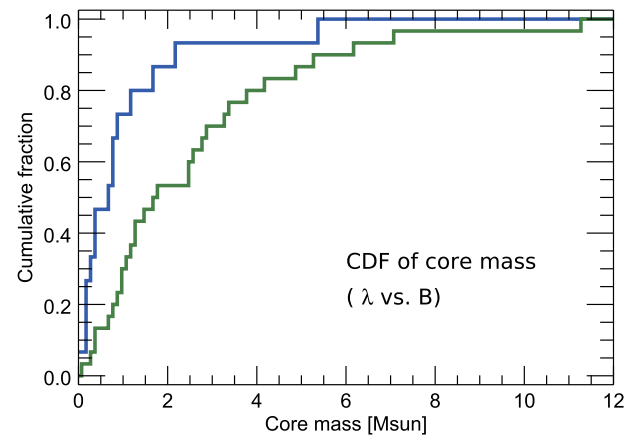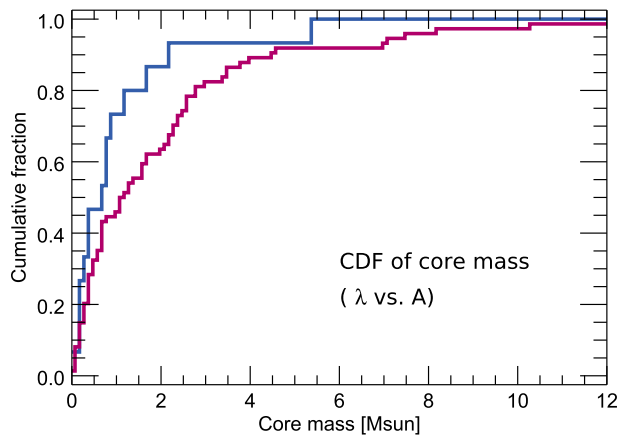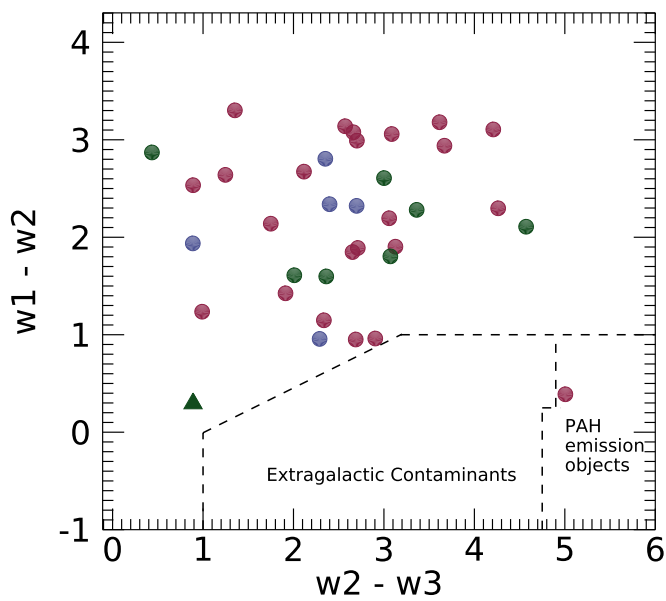
Figure 6. (Continued.)

Figure 7. *WISE* color–color diagram for separating the star-forming galaxies from our YSO candidates. The dashed line shows the criterion for star-forming galaxies and PAH emission objects, and the circles represent our YSO candidates. Different colors denote different regions (blue: λ Orionis cloud; magenta: the Orion A cloud; green: the Orion B cloud) where the YSO candidates are located.
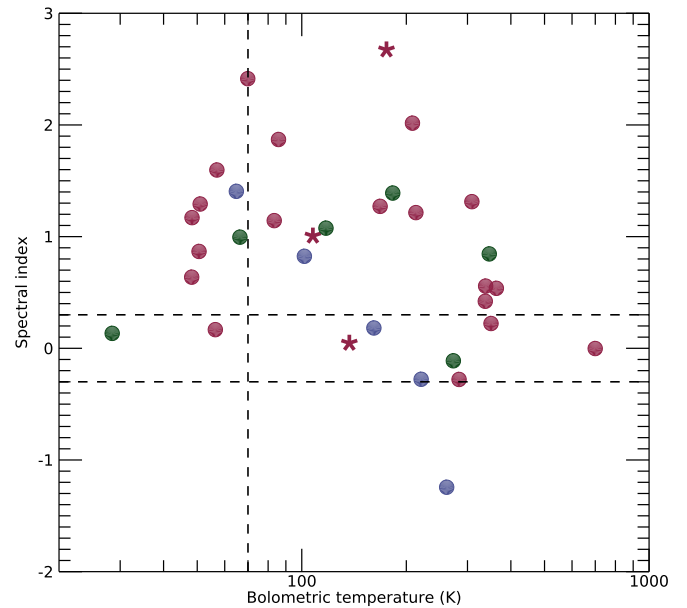
Figure 8. The 3.6–22 μm spectral index $\alpha_{3.6-22}$ versus the bolometric temperature ($T_{\rm bol}$) are plotted for the 64 YSOs in our sample. The dashed lines delineate the regions that define the classifications (see the text for details). The colors are the same as in Figure 7. The asterisks are YSOs calculated with *WISE* and SCUBA-2 data, while the circles are YSOs calculated including far-infrared data.

Table 7
Physical Properties of PGCCs from the PGCC Catalog

Cloud	Number of PGCCs	Median					Mean				
		N_{H_2} $(10^{20}\,cm^{-2})$	T_d (K)	β	n_{H_2} $(10^2\,cm^{-3})$	M_{clump} $(M_\odot)$	N_{H_2} $(10^{20}\,cm^{-2})$	T_d (K)	β	n_{H_2} $(10^2\,cm^{-3})$	M_{clump} $(M_\odot)$
λ Orionis	177	3.2	16.1	1.7	2.2	4.9	6.4	16.0	1.6	4.7	8.5
Orion A	135	10.9	13.4	2.1	6.6	13.8	28.1	13.8	2.0	18.3	30.8
Orion B	154	6.4	13.9	2.0	4.1	7.7	13.4	14.0	1.9	9.1	16.8

gravitationally unstable starless cores are found in the Orion B cloud (100%) and in the λ Orionis cloud (60%), respectively.

3.4. Dense Gas Fraction

To compare the potential of star formation in the three clouds of the Orion complex, we determine the fraction of dense gas, from which stars form, in PGCCs. Submillimeter dust continuum observations with ground-based bolometer arrays filter out the large-scale diffuse gas. Therefore, the ratio between the masses derived from the *Planck* data (at 857, 545, and 353 GHz) combined with the 3 THz *IRAS* data and from the SCUBA-2 850 μm emission represents the dense gas fraction in the cold clump. The core masses are calculated from the SCUBA-2 850 μm images as described in Section 3.3.1, and the clump masses are adopted from the PGCC catalog. Since some PGCCs have no information about masses in the catalog, we adopt a 3σ limit for the flux at 353 GHz and estimate the upper limit of the clump masses. As shown in Figure 10, the dense gas fraction is the highest in the Orion B cloud (0.20) and the lowest in the λ Orionis cloud (0.10). In the Orion A cloud, the fraction is about 0.12.

In the right panel of Figure 10, PGCCs that are not detected at 850 μm are plotted together; the detected PGCCs and non-detected PGCCs are clearly divided into two groups. For the non-detected PGCCs, we calculated the upper limit of core mass, adopting 3σ noise of 850 μm images. The median clump masses of detected PGCCs are higher than those of non-detected PGCCs by factors of 1.6–2.2 in the three clouds. The difference in clump mass between detected and non-detected PGCCs is the greatest (a factor of 2.2) in the λ Orionis cloud. The median column density ($4.9 \times 10^{21}\,cm^{-2}$) and number density ($2.8 \times 10^3\,cm^{-3}$) of the detected PGCCs are higher by factors of 4.9 and 5.4, respectively, compared to those of non-detected PGCCs. Other parameters provided by the PGCC catalog, such as the warm background temperature, do not show a clear difference.

4. Discussion

4.1. The Effect of Stellar Feedback on PGCCs in the λ Orionis Cloud

The λ Orionis cloud provides a good example for showing the effect of a nearby massive star on the core properties. The decrease of dust temperatures of PGCCs along the projected distance from λ Ori suggests that the central star has great influence on the PGCCs, as presented in Figure 11. In Table 7, the physical properties of PGCCs from the PGCC catalog are listed; compared to the PGCCs in the Orion A and Orion B clouds, the PGCCs in the λ Orionis cloud have smaller column and volume densities, and clump masses. Therefore, the lower values of physical properties such as core mass, density, and
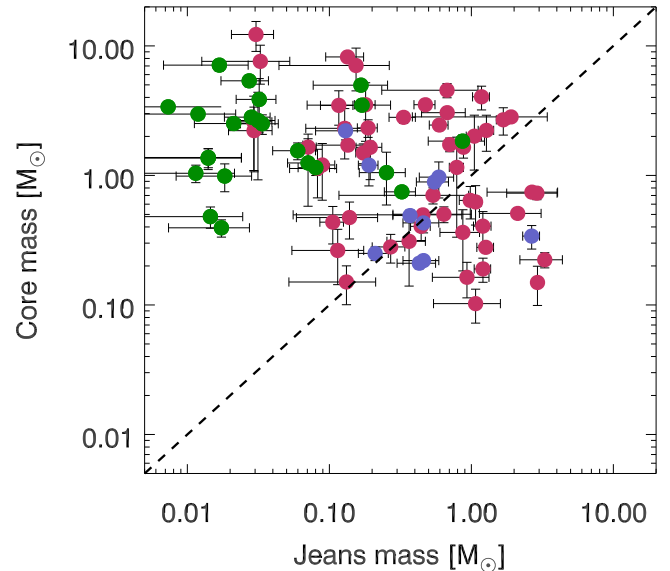

Figure 9. Jeans masses versus core masses for 88 starless cores. The blue, magenta, and green circles represent 10 cores in the λ Orionis, 53 cores in the Orion A, and 25 cores in the Orion B clouds, respectively.

size in the λ Orionis cloud, compared to the Orion A and B clouds, may indicate a strong stellar feedback such as erosion or even destruction of the cores by photoionizing radiation. As shown in Figure 1, the λ Orionis cloud is dominated by Hα emission, indicating that it is shaped by the ionized hydrogen content of a gas cloud. The median dust temperature (16.08 K) of PGCCs in the λ Orionis cloud is higher than those (13–14 K) in the other two clouds. This also suggests the PGCCs in the λ Orionis cloud are externally heated.

The other effect of stellar feedback in the λ Orionis cloud is the unbounding state of the region. Dolan and Mathieu (2001, 2002) interpreted that the shock wave from the supernova explosion dispersed gas at the center of the λ Orionis cloud and left the region unbound. Although most of the PGCCs are located along the ring-shaped structure (see Figure 1), it remains unclear whether they are bound or not. However, we can expect that this region was also affected by supernovae about 1 Myr ago, which may have disrupted the formation of dense and gravitationally bound structures. The recent result showing that the star formation efficiency decreases greatly in less-bound clouds (Lucas et al. 2017) is supported by our result.

Additionally, the dust emissivity spectral index β in the Orion A and B clouds are close to 2, while β in the λ Orionis cloud is much smaller, at 1.65 (see Table 7). Juvela et al. (2015) estimated the β using *Herschel*, *Planck*, and *IRAS* data and found median values over all fields of the *Planck* clumps are 1.84. The β values are well known to be dependent on the physical environments such as grain growth or composition of
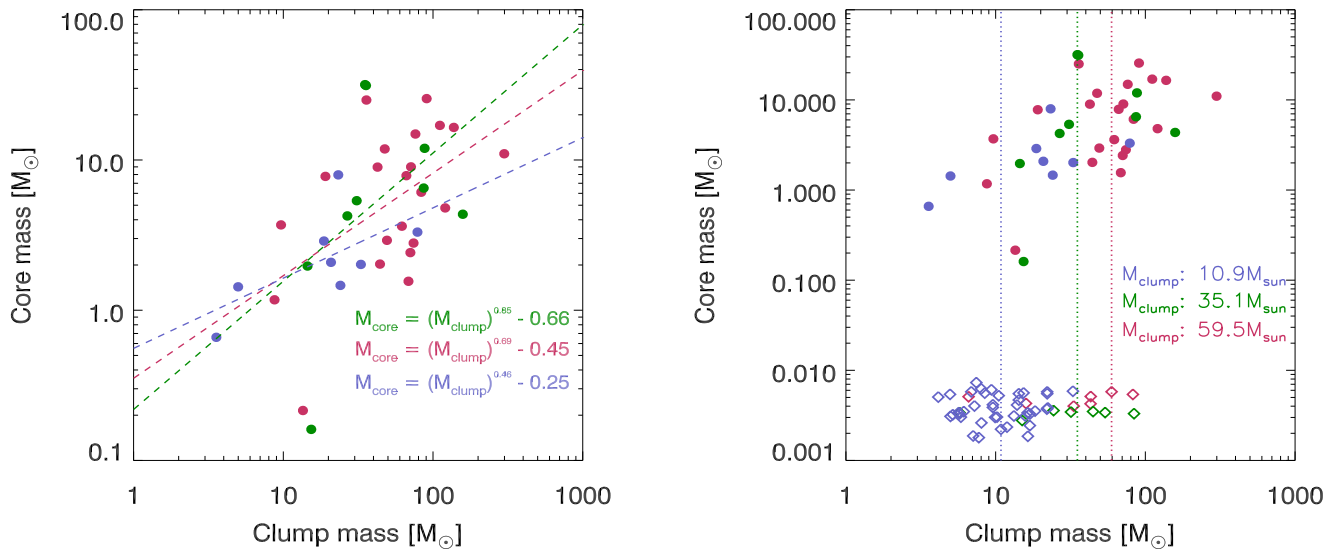
Figure 10. Core masses versus clump masses. Left: The circles represent PGCCs in the λ Orionis cloud (blue), Orion A (magenta), and Orion B (green) clouds, respectively. Each dashed line shows the correlations for each region. Functions in the right lower corner are obtained by fitting. Right: The open diamonds indicate non-detected PGCCs and the colors are the same as those in the left panel. The dotted lines represent median clump masses of λ Orionis, Orion B, and Orion A clouds, respectively.
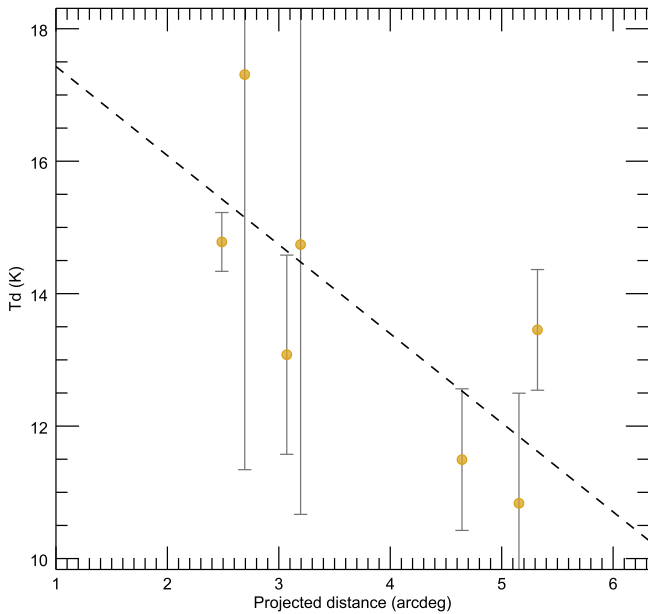
Figure 11. Dust temperature as a function of projected distance from "λ" Ori. The dashed lines show least-squares fit to the data. The eight PGCCs are detected in the λ Orionis cloud, but only seven PGCCs are plotted, the values for which are obtained from the PGCC catalog.

dust grain and evolution of the carbonaceous component (Jones et al. 2013). I-Hsiu Li et al. (2017), however, reported that grain growth may reduce β in circumstellar disks or envelopes only from the late Class 0 stage to the end of the Class I stage of YSOs. Forbrich et al. (2015) also found that β in the inner region of a starless core FeSt 1-457 shows no significant difference from the value for the local cloud, indicating that grain growth does not occur significantly in the very early stage of star formation. The λ Orionis cloud mostly harbors starless cores, and thus β may represent their initial dust property. This result might indicate that the λ Orionis cloud was initially very dense, resulting in vigorous grain growth, and could trigger the massive star formation.

After the explosion of one of O type stars, the PGCCs can be affected by strong radiation. The dust temperature of PGCCs decreases with the projected distance from λ Ori. (see Figure 11). The errors are large, owing to the sensitivity of Planck, but we can see the tendency for dust temperature to decrease with distance. As seen in Table 7, the λ Orionis cloud has a higher median/mean dust temperature and lower median/mean density than other clouds. This may be due to the external heating from the H$_{\rm II}$ region, which can increase the temperature of the molecular cloud, making it hard to cool down to form dense cores. Juvela et al. (2018) investigated properties of β and $T_{\rm d}$ of PGCCs with *IRAS*, *Planck*, SCUBA-2, and *Herschel* data and suggested that the heating effect of a protostar on its environment is very small, because of its small volume compared to the surrounding material. Thus, the embedded protostars should not significantly contribute to raising the dust temperature of their parent clumps in the λ Orionis cloud, supporting the idea that the higher dust temperatures in the λ Orionis cloud are mainly influenced by the external heating. This may also account for the lower column densities of PGCCs in the λ Orionis cloud, because the external radiation can disperse gas via photo-evaporation as well as heating.

4.2. Two Types of Sub-clouds in the λ Orionis Cloud

Dolan and Mathieu (2002) suggested that the original shape of the λ Orionis cloud was like a linear string of dense molecular clouds. The most massive region was the central part of the initial cloud, including B30, B35, the location of today's "λ Ori," and B223 (at the southwest of these). The rest of the cloud was filled by lower density molecular gas. As mentioned previously, the supernova explosion quickly dispersed most of the parent cloud and then swept up molecular gas and dust, creating the ring structure that is seen today. Lang et al. (2000) suggested that the sub-clouds in the λ Orionis cloud were divided into two classes after the supernova explosion, based on their CO $J = 1-0$ survey: (1) dense and massive sub-clouds, and (2) diffuse and low-mass sub-clouds. In the following section, we explore the characteristics of each sub-cloud in the

Table 8
Two Types of Sub-clouds in the λ Orionis Cloud

Sub-cloud	Region	Detection rate of PGCCs (%)	Dense gas fraction	Core mass[a] ($M_\odot$)	N_{H_2} [a] (10^{22} cm^{-2})
Dense and massive	B30, B35	38	0.19	1.68	11.3
Diffuse and low-mass	rest of the cloud	8	0.05	0.96	5.7

Note.
[a] The median value of cores in each sub-cloud.

context of the provided scenarios and summarize the results in Table 8.

4.2.1. Dense and Massive Regions

Dolan and Mathieu (2002) suggested that dense and high-mass regions of the λ Orionis cloud are remaining parts of the initial parent cloud. B30 and B35 support this scenario. They were accompanied by a massive cloud core, which became the birthplace of OB stars, called "λ Ori" today. These two clouds may be massive enough to survive from the supernova explosion.

On the other hand, B223 might not be part of the λ Orionis cloud because it is located at the southwest region away from the central part ("λ Ori," B30 and B35). The pre-main sequence stars in B223 have different radial velocities from those in B30 and B35 (Dolan & Mathieu 2002). In our survey, there are 18 PGCCs in this region, but none of them were detected at 850 μm. This supports the idea that B223 was not originally associated with the λ Orionis cloud, but is just coincidentally projected to the same region of sky as the λ Orionis cloud.

Thirteen PGCCs were observed in two dense clouds (B30 and B35) and the detection rate is about 38% (5 out of 13), about 2.5 times higher than the total detection rate (16%, 8 out of 50) in the λ Orionis cloud. The median mass and column density of the 13 PGCCs are 13.8 $M_\odot$ and 1.3 $\times$ 10^{21} cm^{-2}, respectively. The dense gas fraction, already mentioned earlier, is 0.19, which is comparable to the value for the Orion B cloud. The median column density of detected cores is 1.1 $\times$ 10^{23} cm^{-2}, which is similar to those of Orion A (1.5 $\times$ 10^{23} cm^{-2}) and lower than those of Orion B (3.8 $\times$ 10^{23} cm^{-2}). This result suggests that core formation in dense and massive regions is much less affected by the stellar feedback.

4.2.2. Diffuse and Low-mass Regions

The low-mass and low-density regions may result from the supernova blast and subsequent fragmentation of the molecular ring (Lang et al. 2000; Dolan & Mathieu 2001). We find several indications that core formation is much more depressed in the diffuse and low-mass regions. All properties are lower than those of the dense and massive regions of the λ Orionis cloud and other star-forming regions of the Orion A and B clouds.

The detection rate of the diffuse and low-mass region is about 8% (3 out of 36), which is five times lower than that of dense regions (38%) in the λ Orionis cloud. The dense gas fraction is also the lowest, at 0.05. It is lower by a factor of four compared to the dense and massive regions of the λ Orionis cloud. The median mass and column density of the 36 PGCCs are 13.9 $M_\odot$ and 9.9 $\times$ 10^{20} cm^{-2}, respectively, which are not very different from those of PGCCs in the dense and massive regions (see Section 4.2.1). However, the median mass and column density of cores in this low-density region are 0.96 $M_\odot$

and 5.7 $\times$ 10^{22} cm^{-2}, which are lower than those in the high density region by a factor of two (Table 8). These results imply that after the supernova explosion, the diffuse and low-mass regions are significantly affected by massive stars; core formation was suppressed, and thus the fraction of dense gas became low.

4.3. Multiplicity of the Three Clouds

We have identified a total of 119 cores within 40 PGCCs, as previously discussed. The averaged multiplicity (number of cores in one PGCC) for the three clouds is nearly 3. Figure 12 shows histograms of multiplicity, column density, and mass of PGCCs, respectively. The multiplicity in the λ Orionis is less than 2 (15 cores within 8 PGCCs), but for Orion A (74 cores within 23 PGCCs) and B (30 cores within 9 PGCCs), the multiplicities are significantly larger than 3 (see also Tables 2 to 4). This clear difference is obvious in Figure 3 to Figure 5. In Figure 12, the column densities and masses of PGCCs in the λ Orionis cloud occupy the bins of lower values, while PGCCs in the Orion A and B clouds show wide distributions. The difference of multiplicity in the λ Orionis cloud can arise from the strong radiation field. The UV photons from the OB association in the λ Orionis cloud heat the clumps externally and hinder them from cooling. Therefore, the clumps are difficult to collapse and fragment.

In Figure 6, we plot the cumulative mass and column density fraction of cores in the three clouds. The two profiles of each panel are strikingly different. The λ Orionis cloud has substantially lower fractions of core mass and column density than those of Orion A and B clouds. We also found that the mean and median clump masses and volume densities are the lowest in the λ Orionis cloud. This is in line with results of Polychroni et al. (2013) indicating that clumps within filaments have higher masses than clumps outside of the filaments. The entire structure of molecular clouds of Orion A and B are filamentary, while λ Orionis is a ring-shaped structure (Figures 1 and 2). This discrepancy can provide a significant clue concerning the physical origin of the environmental conditions between the λ Orionis cloud and Orion A and B clouds.

The fragmentation of clumps, which increases multiplicity, also might be caused by non-thermal motions, such as turbulence, which could be manifested by line broadening by bulk motions. We conducted single dish observations (H.-W. Yi et al., in preparation) using Korean VLBI Network and found that the line widths are meaningfully broader in cores of Orion A and B than cores in the λ Orionis cloud. The median FWHM of both HCN ($J = 1 \rightarrow 0$) and H_2CO ($2_{1,2} \rightarrow 1_{1,1}$) are the largest in Orion B as 1.40 km s^{-1}, and the FWHM of C_2H ($N = 1 \rightarrow 0$) is the largest in the Orion A as 1.14 km s^{-1}. The median FWHMs of HCN, H_2CO, and C_2H in the λ Orionis clouds are 0.87, 1.00, and 0.78 km s^{-1}, respectively. These are the lowest median values among the three clouds. This result
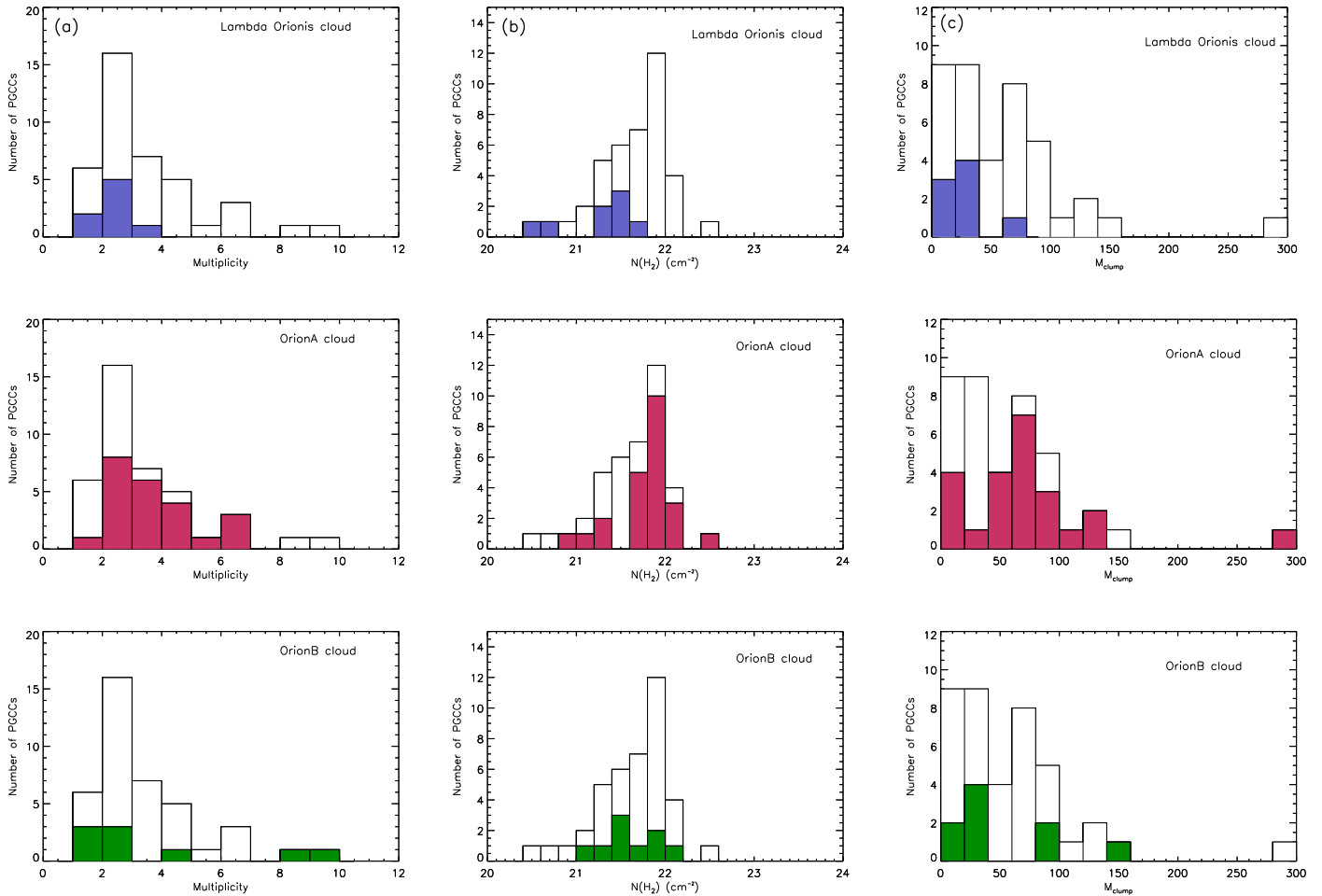
Figure 12. Histograms of the multiplicity (a), column density (b), and mass (c) for the 40 PGCCs detected at SCUBA-2 850 μm dust continuum in this work. Different colors denote different regions as used in previous figures, and open histograms indicate the total number of PGCCs in each bin.

may support that greater internal motions of turbulence actively led to the fragmentation of clumps down to cores in the Orion A and B clouds.

5. Summary

We investigated the physical properties of all the 96 PGCCs in three clouds of the Orion complex using the JCMT/ SCUBA-2 850 μm continuum data. In total, 58 out of 96 PGCCs were observed as part of the SCOPE survey and the rest of 38 PGCCs were studied with archival data.

We identified 119 cores within the detected 40 PGCCs; 34 cores are protostellar, while 85 cores are starless. To examine the gravitational instability of starless cores, we estimated their Jeans masses. In the Orion A cloud, 37 out of 52 starless cores have masses larger than their Jeans masses, and they may collapse to form protostars. In case of the Orion B cloud, all the 23 starless cores have masses larger than their Jeans masses. In the λ Orionis cloud, 40% (four out of ten) of the starless cores remain gravitationally unbound and thus may be finally dispersed. The rest of 60% starless cores may collapse to form protostars.

Additionally, we explore the characteristics of each sub-cloud in the λ Orionis cloud following a scenario of Lang et al. (2000). The cores in the dense and massive regions show comparable column density (1.1×10^{23} cm^{-2}) to that of Orion A cloud (1.5×10^{23} cm^{-2}), while the cores in the diffuse and low-mass regions show the lowest median column density of

5.7×10^{22} cm^{-2}. This difference suggests that after the supernova explosion, the diffuse and low-mass regions are significantly affected by massive stars; core formation was suppressed, and thus the fraction of dense gas became low.

We compared the overall properties of PGCCs in the λ Orionis cloud with those of PGCCs in the Orion A and Orion B clouds, and we found PGCCs in the λ Orionis cloud usually have higher $T_{\rm dust}$, suggesting that PGCCs in the λ Orionis cloud are externally heated. In addition, high energy photons from the massive star (λ Ori) can photo-evaporate the dense material and lead to lower column densities in the λ Orionis cloud. This effect can also cause the lower multiplicity in the λ Orionis cloud (1.8) compared to that of Orion A (3.2) and B (3.3) clouds. Among three clouds, the cores in the λ Orionis cloud have the lowest median values of the mass (0.77 $M_{\odot}$), size (0.09 pc), column density (8.2×10^{22} cm^{-2}), volume density (2.5×10^5 cm^{-3}), and dense gas fraction (0.10). Therefore, we conclude that a massive star gave negative feedback to the core formation and evolution in the λ Orionis cloud.

ORCID iDs

Jeong-Eun Lee ⓘ https://orcid.org/0000-0003-3119-2087
Tie Liu ⓘ https://orcid.org/0000-0002-5286-2564
Kee-Tae Kim ⓘ https://orcid.org/0000-0003-2412-7092
Gary Fuller ⓘ https://orcid.org/0000-0001-8509-1818
Sung-ju Kang ⓘ https://orcid.org/0000-0002-5004-7216
P. Koch ⓘ https://orcid.org/0000-0003-2777-5861
Chang Won Lee ⓘ https://orcid.org/0000-0002-3179-6334
Di Li ⓘ https://orcid.org/0000-0003-3010-7661
Patrico Sanhueza ⓘ https://orcid.org/0000-0002-7125-7685
Archana Soam ⓘ https://orcid.org/0000-0002-6386-2906
Ken'ichi Tatematsu ⓘ https://orcid.org/0000-0002-8149-8546
Ke Wang ⓘ https://orcid.org/0000-0002-7237-3856
Glenn J. White ⓘ https://orcid.org/0000-0002-7126-691X
Yuefang Wu ⓘ https://orcid.org/0000-0002-5076-7520
Yao-Lun Yang ⓘ https://orcid.org/0000-0001-8227-2816

References

Adams, F. C., Lada, Ch. J., & Shu, F. H. 1987, ApJ, 312, 788
Andre, P., & Montmerle, T. 1994, ApJ, 420, 837
Bergin, E. A., & Tafalla, M. 2007, ARA&A, 45, 339
Bintley, D., Holland, W. S., MacIntosh, M. J., et al. 2014, Proc. SPIE, 9153, 915303
Buckle, J. V., Davis, C. J., Francesco, J. D., et al. 2012, MNRAS, 422, 521
Chambers, E. T., Jackson, J. M., Rathborne, J. M., & Simon, R. 2009, ApJS, 181, 360
Chen, H., Myers, P. C., Ladd, E. F., & Wood, D. O. S. 1995, ApJ, 445, 377
Cunha, K., & Smith, V. V. 1996, A&A, 309, 892
Dolan, C. J., & Mathieu, R. D. 2001, AJ, 121, 2124
Dolan, C. J., & Mathieu, R. D. 2002, AJ, 123, 387
Dunham, M. M., Stutz, A. M., Allen, L. E., et al. 2014, in Protostars & Planets VI, ed. H. Beuther et al. (Tucson, AZ: Univ. Arizona Press), 195
Evans, N. J., II, Dunham, M. M., Jørgensen, J. K., et al. 2009, ApJS, 181, 321
Forbrich, J., Rodríguez, L. F., Palau, A., et al. 2015, ApJ, 814, 15
Furlan, E., Fischer, W. J., Ali, B., et al. 2016, ApJS, 224, 5
Galli, D., Walmsley, M., & Gonçalves, J. 2002, A&A, 394, 275
Goldreich, P., & Kwan, J. 1974, ApJ, 189, 441
Goldsmith, P. F., Pineda, J. L., Langer, W. D., et al. 2016, ApJ, 824, 141
Holland, W. S., Bintley, D., Chapin, E. L., et al. 2013, MNRAS, 430, 2513
I-Hsiu Li, J., Liu, H. B., Hasegawa, Y., & Hirano, N. 2017, ApJ, 840, 72
Jeffries, R. D. 2007, MNRAS, 376, 1109
Jones, A. P., Fanciullo, L., Köhler, M., et al. 2013, A&A, 558, A62
Jørgensen, J. K., Johnstone, D., Kirk, H., & Myers, P. C. 2007, ApJ, 656, 293
Juvela, M., Demyk, K., Doi, Y., et al. 2015, A&A, 584, A49
Juvela, M., He, J., Pattle, K., et al. 2018, A&A, 612, 71
Kim, J., Lee, J.-E., Liu, T., et al. 2017, ApJS, 231, 9
Koenig, X. P., & Leisawitz, D. T. 2014, ApJ, 791, 131
Kryukova, E., Megeath, S. T., Gutermuth, R. A., et al. 2012, AJ, 144, 31
Lada, Ch. J. 1987, in Proc. IAU Symp. 115, Star Forming Regions, ed. M. Peimbert & J. Jugaku (Dordrecht: Reidel), 1
Lang, W. J., Masheder, M. R. W., Dame, T. M., & Thaddeus, P. 2000, A&A, 357, 1001
Liu, T., Kim, K.-T., Juvela, M., et al. 2018a, ApJS, 234, 28
Liu, T., Li, P. S., Juvela, M., et al. 2018b, ApJS, in press (arXiv:1803.09457)
Liu, T., Wu, Y., & Zhang, H. 2012, ApJS, 202, 4
Liu, T., Zhang, Q., Kim, K.-T., et al. 2016, ApJS, 222, 7
Lucas, W. E., Bonnell, I. A., & Forgan, D. H. 2017, arXiv:1701.04414
Megeath, S. T., Gutermuth, R., Muzerolle, J., et al. 2012, AJ, 144, 192
Myers, P. C., & Ladd, E. F. 1993, ApJL, 413, L47
Perryman, M. A. C., Lindegren, L., Kovalevsky, J., et al. 1997, A&A, 323, L49
Planck Collaboration, Ade, P. A. R., Aghanim, N., et al. 2016, A&A, 594, A28
Polychroni, D., Schisano, E., Elia, D., et al. 2013, ApJL, 777, L33
Sandstrom, K. M., Peek, J. E. G., Bower, G. C., Bolatto, A. D., & Plambeck, R. L. 2007, ApJ, 667, 1161
Stutz, A. M., Tobin, J. J., Stanke, T., et al. 2013, ApJ, 767, 36
Tatematsu, K., Liu, T., Ohashi, S., et al. 2017, ApJS, 228, 12
Tang, M., Liu, T., Qin, S.-L., et al. 2018, ApJ, 856, 141
Tobin, J. J., Stutz, A. M., Megeath, S. T., et al. 2015, ApJ, 798, 128
Wang, K., Zhang, Q., Testi, L., et al. 2014, MNRAS, 439, 3275
Williams, J. P., Blitz, L., & McKee, C. F. 2000, in Protostars and Planets IV, ed. V. Mannings, A.P. Boss, & S.S. Russell (Tucson, AZ: Univ. of Arizona Press), 97
Williams, J. P., de Geus, E. J., & Blitz, L. 1994, ApJ, 428, 693
Wilson, B. A., Dame, T. M., Masheder, M. R. W., & Thaddeus, P. 2005, A&A, 430, 523
Wright, E. L., Eisenhardt, P. R. M., Mainzer, A. K., et al. 2010, AJ, 140, 1868